Planetary and Space Science 260 (2025) 106100

Contents lists available at ScienceDirect

Planetary and Space Science

journal homepage: www.elsevier.com/locate/pss

Diurnal temperature cycle models and performances on Martian surface using in-situ and satellite data

Yu Wang [a,b], Shuanggen Jin [a,c,*]

[a] Shanghai Astronomical Observatory, Chinese Academy of Sciences, Shanghai, 200030, China
[b] School of Astronomy and Space Science, University of Chinese Academy of Sciences, Beijing, 100049, China
[c] School of Surveying and Land Information Engineering, Henan Polytechnic University, Jiaozuo, 454003, China

ARTICLE INFO

Keywords:
Martian surface temperature
Diurnal temperature cycle model
In-situ observations
Parameter-reduction approach

ABSTRACT

Martian surface temperature and its diurnal variations play a key role in studying Mars land-atmosphere interactions. However, accurate Diurnal Temperature Cycle (DTC) models on Martian surface are presently absent or have large uncertainties. This study aims to construct semi-empirical DTC models of the Martian surface and address this gap by assessing their performances. Utilizing in-situ data collected by the Viking 1, Insight, Perseverance, and Curiosity rovers, we assess the performances of these DTC models by examining overall accuracy, daily precision, error rates across various hours, and effectiveness during different Martian seasons. The parameters of the models gain insights into the seasonal variations of surface temperature on Mars. Additionally, we conduct a focused analysis on the parameter-reduction approaches (PRAs) to assess the potential suitability of DTC models with the constraints of limited satellite observations available for Mars. Results indicate that the DTC models can effectively capture the diurnal surface temperature variations on Mars, with an overall error ranging from 0.74 to 2.28 K. Among the DTC models, the DMT24 model developed in this study shows the superior performance and can reproduce the slow and smooth increase around sunrise and maintain accuracy during nighttime periods. The DTC models can well capture the diurnal surface temperature cycle on Mars using limited satellite data based on suitable PRAs. This study offers valuable references for utilizing global DTC models on Mars.

1. Introduction

Martian surface temperature is a crucial parameter in comprehending climate changes on Mars, particularly in evaluating the presence of surface water ice (Grima et al., 2009; Stcherbinine et al., 2023), subsurface water (Bandfield, 2007; Li et al., 2023), environmental evolution (Jin and Zhang, 2014), and the habitability of Mars (Michalski et al., 2018) as well as the possibility of life (Mellon et al., 2024). Surface temperature plays an integral role in land-atmosphere interactions, which governs the characteristics of convective activity in the atmospheric surface layer and determines the extent of the planetary boundary layer with influencing key atmospheric dynamics (Li et al., 2021; Smith et al., 2017). The importance of Martian surface temperature becomes particularly prominent due to the tenuous atmosphere of Mars, which lacks the moderating influence in more substantial atmospheres (Munguira et al., 2023). Variations in the Martian surface temperature give rise to global oscillations in atmospheric pressure, temperature, and winds. These fluctuations play a pivotal role in shaping dust events (Wolfe et al., 2023; Xiao et al., 2019) and constitute the core dynamics of the Martian polar caps (Arnold et al., 2022; Piqueux et al., 2008). Furthermore, the diurnal cycle of Martian surface temperature is instrumental in estimating the energy and mass exchanges occurring at the land-atmosphere boundary (Atri et al., 2023; Martínez et al., 2014). These interactions are key determinants of the heat flux transmitted from the surface to the planetary boundary layer, thereby exerting a substantial influence on the weather and climate on Mars.

Several missions have proven their capacity to reliably acquire surface temperature measurements on Mars. For instance, the Thermal Emission Spectrometer (TES) provided the first systematic mapping of the Martian global thermal structure (Smith, 2008) and offered invaluable data for analyzing seasonal and annual temperature variations on Mars (Smith, 2004). The Mars Odyssey's Thermal Emission Imaging System (THEMIS) operated since 2003 has amassed data spanning over

* Corresponding author. Shanghai Astronomical Observatory, Chinese Academy of Sciences, Shanghai, 200030, China.
E-mail address: sgjin@shao.ac.cn (S. Jin).

https://doi.org/10.1016/j.pss.2025.106100
Received 17 June 2024; Received in revised form 10 February 2025; Accepted 19 March 2025
Available online 20 March 2025

two decades (equivalent to ten Martian years), significantly augmenting our understanding of the Martian surface climate (Smith, 2019a; Smith et al., 2003). Its concurrent operation with TES for five years enabled essential cross-calibration of atmospheric measurements, enriching the reliability and accuracy of the data (Christensen et al., 2004). Further advancements were made with the deployment of subsequent instruments like the Planetary Fourier Spectrometer (PFS) aboard Mars Express (Giuranna et al., 2021; Helbert et al., 2006; Wolkenberg et al., 2011) and the Mars Climate Sounder (MCS) on the Mars Reconnaissance Orbiter (MRO) (Kleinböhl et al., 2009; McCleese et al., 2007). These missions have enhanced the quality of data, offering a more comprehensive understanding of the Martian surface and atmospheric conditions. In-situ observations have also yielded a wealth of invaluable data. The Viking Landers, as pioneers in delivering in-situ meteorological data from the Martian surface, unveiled the significant thermal amplitude of the diurnal temperature cycle (Hess et al., 1977; Sutton et al., 1978). The Pathfinder mission, with its multi-level temperature measurements, provided deeper insights into the heat and momentum exchange between the Martian atmosphere and surface (Schofield et al., 1997). Additionally, the Phoenix lander, positioned at 68°N within the Martian arctic, has contributed valuable data from its unique location (Davy et al., 2010). Recent rover missions like Curiosity (Savijärvi et al., 2022), Insight (Banfield et al., 2020), and Perseverance (Rodriguez-Manfredi et al., 2023) have perpetuated the exploration on Mars, recording surface temperature data multiple seasons, including periods of dust storms. Each mission has significantly contributed to our comprehension of Martian surface temperatures, enriching our knowledge of Martian atmospheric and surface dynamics.

Satellite remote sensing is highly effective in measuring surface temperatures across extensive areas. However, a tradeoff exists between the spatial and temporal resolutions in the majority of satellite observations. This compromise often leads to a temporally discontinuous or even sporadic sampling of the surface. Fortunately, Diurnal Temperature Cycle (DTC) models provide a solution to this challenge. Among the DTC models, the semi-empirical model (SEM) prevails because of its direct description of surface temperature, inherent simplicity, and a relatively limited parameter range (three to six parameters). Through fitting a DTC model, a set of parameters describing the thermal dynamics of the land surface is obtained. Once these parameters are determined, the surface temperature at any time of the day can be described. These models have demonstrated their efficacy in reconstructing spatio-temporally continuous surface temperatures (Hong et al., 2022), estimating surface air temperatures (Bechtel et al., 2014, 2017), deducing surface thermal properties (Holmes et al., 2015), and identifying soil freeze/thaw status on Earth (Zhan et al., 2014). Nonetheless, a compromise exists between modeling precision and the parameter count of DTC models. DTC models with a greater number of parameters typically yield heightened accuracies (Duan et al., 2012; Huang et al., 2014). However, models with excessive parameters are impractical for satellite measurements due to the constraints of limited observations. Therefore, parameter reduction approaches (PRAs) have received special attention. By reducing parameters in existing DTC models, a DTC model with an appropriate number of parameters for satellite data can be facilitated (Duan et al., 2014; Hong et al., 2018; Schädlich et al., 2001).

Mars possesses an atmosphere analogous to that of Earth, but there are distinct differences between the Martian atmosphere and its terrestrial counterpart (Banerdt et al., 2020; Kavulich et al., 2013; Temel et al., 2022). Most studies have used physics-based models, such as THM, to simulate diurnal cycles by adjusting parameters like albedo and thermal inertia to achieve the best-fit cycle that matches observations (Martínez et al., 2021; Vasavada et al., 2017). However, the effectiveness of these semi-empirical DTC models in Martian conditions remains uncertain. There is aslo a lack of comprehensive assessment regarding the performance of these semi-empirical DTC models, as well as the PRAs. To address these issues, in this paper, we conducted a comparative analysis of the performance of DTC models on Mars using in-situ measurements collected from Viking1, Insight, Perseverance, and Curiosity rovers. The characteristics of parameters are further scrutinized to facilitate a deeper comprehension of these models as applied to Mars. Additionally, PRAs were evaluated to simulate the condition of limited data obtained from satellite observations.

The structure of the paper is organized as following. In-situ observations and satellite data employed in this study are outlined in Section 2. The methodology for modeling the Martian surface temperature is detailed in Section 3. Results and analysis are presented in Section 4, including an examination of the efficacy of DTC models using in-situ data, a detailed analysis of model parameter characteristics, and an evaluation of DTC model performance utilizing satellite data. Section 5 contains discussions on the results and outlines future work. Conclusions are given in Section 6.

2. Observation data

2.1. In-situ data

Currently, there is a limited amount of in-situ data available for Mars. For our analysis, we use data collected by four rovers: Viking 1, Insight, Perseverance, and Curiosity. These rovers operated over a Martian year, allowing us to evaluate performance across different locations whenever feasible. The detailed information on these in-situ data is listed in Table 1.

2.1.1. Viking mission

The Viking landers represent a pioneering pair of spacecraft deployed to explore Mars, marking the first successful landings on the Martian surface with the primary objective of investigating potential signs of past or present life (Hess et al., 1972; Moore et al., 1987). Following their respective arrivals on July 20 (Lander 1) and September 3 (Lander 2) in 1976, these two landers operated continuously for nearly four Martian years (Moore et al., 1987; Soffen, 1976, 1977; Soffen and Snyder, 1976). Although the footpad sensor was not specifically designed to necessarily survive (Tillman, 1989), it provided valuable in-situ surface temperature data on Mars. It should be noted that the footpad sensor of Viking1 was buried by soil about 0.165 m below the surface (Moore et al., 1977).

2.1.2. Insight

On November 26, 2018, the InSight mission achieved a successful landing on Mars within the Elysium Planitia region. Its primary goal is to deepen our understanding of the formation and evolution processes of terrestrial planets by investigating the interior structure of Mars (Banerdt et al., 2020). Onboard InSight, the Radiometer (RAD) comprises a suite of radiometers specifically designed to measure surface temperatures by conducting radiance measurements at three wavelength windows (Piqueux et al., 2021). Its performance is characterized by a random measurement error equivalent to 4 K at 150 K (Spohn et al., 2018). Two sets of three RAD units are mounted on Insight. One set observes the soil in close proximity to the lander. The other set monitors the surface approximately 3.5 m away from the nearest edge of the deck (Mueller et al., 2021). In this study, we employ the mean surface temperature obtained from two sets of instruments to address discrepancies that may arise from observations conducted at a single site.

Table 1
Description of in-situ Mars surface temperature data.

Rover name	Latitude	Longitude	Instrument	Sols
Viking 1	22.3 °N	312.0 °E	Footpad sensor	740
Insight	4.5 °N	135.9 °E	RAD	360
Perseverance	18.4 °N	77.5 °E	TIR	826
Curiosity	4.6 °S	137.4 °E	REMS	3503

2.1.3. Perseverance

The Perseverance rover landed on Mars at Jezero crater on February 18, 2021 (Farley et al., 2020). Onboard Perseverance, the Mars Environmental Dynamics Analyzer (MEDA) comprises a collection of meteorological sensors designed to measure pressure, temperature, wind speed, and relative humidity on Mars (Smith et al., 2023). TIRS, a component of the MEDA suite, consists of an infrared radiometer featuring five channels for measuring various parameters: downward longwave radiation (IR1), air temperature at 40 m (IR2), upward short-wave radiation (IR3), upward longwave radiation (IR4) and surface temperature (IR5). The surface temperature data obtained via TIRS achieves an accuracy of 0.75 K with a resolution of 0.08 K (Rodriguez-Manfredi et al., 2021; Sebastián et al., 2021).

2.1.4. Curiosity

In August 2012, the Curiosity rover landed in Gale Crater with the goal of comprehending the past and present habitability of its designated area (Martínez et al., 2017). The Mars Science Laboratory (MSL) mission, aimed at studying the climate, water, and CO2 cycles on Mars, has far exceeded its operational goal and has provided the longest-running surface meteorological dataset on Mars (Vasavada, 2022). The Rover Environmental Monitoring Station (REMS) instrument suite measures atmospheric pressure, air temperature, ground temperature, relative humidity, wind speed, wind direction, and ultraviolet radiation (Gómez-Elvira et al., 2012, 2014). The Ground Temperature Sensor (GTS) on REMS records the infrared brightness temperature of the Martian surface using three thermopiles. It provides ground brightness temperature data with an accuracy of ±1 K at 273 K (Gómez-Elvira et al., 2014).

2.2. Satellite data

MCS and THEMIS, two instruments capable of providing valuable surface temperature data from Mars orbit, are chosen to simulate the practical scenario of utilizing satellite-derived data to model the temporally continuous surface temperature of Mars.

2.2.1. MCS

The Mars Reconnaissance Orbiter (MRO) spacecraft (Zurek and Smrekar, 2007) carries the MCS instrument (McCleese et al., 2007), which consists of a 9-channel infrared radiometer. This instrument enables observations of the Martian surface and atmosphere from various angles, including limb, off-nadir, and nadir orientations. The MCS offers temperature profiles from the surface up to an altitude of 80 km. These profiles have a vertical resolution of 5 km and are available at local times approximately around 03:00 and 15:00. This capability facilitates global monitoring of atmospheric properties, including atmospheric circulation, seasonal variations, and interannual climate variability (Shirley et al., 2015). The precision of the retrieved temperatures is estimated to range from 0.5 to 2 K (Kleinböhl et al., 2009).

2.2.2. THEMIS

The THEMIS instrument (Christensen et al., 2004) consists of cameras capable of imaging Mars across both thermal infrared and visible wavelengths. Its primary objectives include determining surface mineralogy and investigating small-scale geologic processes and thermophysical properties. In this study, which focuses on surface temperature, we utilize THEMIS band 3 (centered at 7.93 μm) to estimate the Martian surface temperature. Band 3 is chosen for its transparency and the ability to quickly approximate using brightness temperature (Smith, 2019a). With typical daytime surface temperatures around 245 K, THEMIS thermal-infrared images exhibit a single-pixel noise equivalent delta temperature of 0.4 K at 9.35 μm (Smith et al., 2003). The local times observed by THEMIS varied between approximately 2:45/14:45 and 7:30/19:30 over the long duration of the Odyssey mission (Smith, 2019b).

3. Models and methodology

3.1. DTC models

Four semi-empirical DTC models of the Martian surface are evaluated: GOT01 (Göttsche and Olesen, 2001), VAN06 (Van den Bergh et al., 2006), INA08 (Inamdar et al., 2008), and GOT09 (Göttsche and Olesen, 2009). Furthermore, an enhanced Diurnal Martian Temperature model, denoted as DMT24, is developed to refine the characterization of Martian surface temperatures. These models employ empirical functions to depict variations in surface temperature, each with parameter numbers from five to six.

3.1.1. GOT01 model

Göttsche and Olesen (2001) proposed a two-part DTC model to describe the diurnal temperature variations under clear-sky conditions. This model delineates the evolution of daytime surface temperature through the utilization of a cosine function, while nighttime temperature decay is characterized by an exponential function, assuming adherence to Newton's law of cooling for surfaces. Here is a detailed description of the model:

$$\mathrm{T_d}(\mathrm{t}) = \mathrm{T_0} + \mathrm{T_a}\cos\left(\frac{\pi}{\omega}(\mathrm{t}-\mathrm{t_m})\right), \mathrm{t} < \mathrm{t_s} \tag{1}$$

$$T_n(t) = (T_0 + \delta T) + \left[T_a \cos\left(\frac{\pi}{\omega}(t_s - t_m)\right) - \delta T\right] e^{\frac{-(t-t_s)}{k}}, t \geq t_s \tag{2}$$

where $\mathrm{T_d}$ and T_n denote the temperature at the daytime and nighttime, respectively. T_0 is the residual temperature around sunrise, $\mathrm{T_a}$ is the temperature amplitude, ω is the width over the half-period of the cosine term, t_m is the time when the temperature reaches its maximum, t_s is the time when free attenuation begins, δT is the day-to-day change of residual temperature, k is the attenuation constant. The values of ω can be determined by the duration of daytime (DD), and the k can be derived by requiring the two parts of the model to be first differentiable at $t = t_s$. They are calculated by:

$$\omega = \frac{2}{15}\arccos(-\tan\phi\tan\delta) \tag{3}$$

$$k = \frac{\omega}{\pi}\left[\tan^{-1}\left(\frac{\pi}{\omega}(t_s - t_m)\right) - \frac{\delta T}{T_a}\sin^{-1}\left(\frac{\pi}{\omega}(t_s - t_m)\right)\right] \tag{4}$$

where ϕ is the latitude, and δ is the solar declination.

Hence, the GOT01 model contains five free parameters (T_0, $\mathrm{T_a}$, t_m, t_s, δT), necessitating a minimum of five LST observations within a day to estimate these parameters accurately.

3.1.2. VAN06 model

Van den Bergh et al. (2006) observed that the width of the best-fitting cosine term of the DTC differed between the rising slope in the morning and the falling slope in the afternoon. As a result, they proposed a DTC model that introduced an additional term based on the GOT01 model. This model encompassed three functions representing the entire DTC: one for the rising slope of the daytime curve, another for the falling slope of the daytime curve, and a third term describing nighttime cooling. The model can be expressed as follows:

$$T_{d1}(t) = T_0 + T_a\cos\left(\frac{\pi}{\omega_1}(t - t_m)\right), t < t_m \tag{5}$$

$$T_{d2}(t) = T_0 + T_a\cos\left(\frac{\pi}{\omega_2}(t - t_m)\right), t_m \leq t < t_s \tag{6}$$

$$T_n(t) = T_0 + T_a\cos\left(\frac{\pi}{\omega_2}(t_s - t_m)\right)e^{\frac{-(t-t_s)}{k}}, t \geq t_s \tag{7}$$

where T_{d1} and T_{d2} denote the daytime temperature before and after reaching its maximum, respectively. ω_1 and ω_2 are widths of the cosine terms for morning and afternoon, respectively. T_n T_0, T_a, t_m, t_s have the same definitions as in the GOT01 model. Therefore, the VAN06 model involves six free parameters (T_0, T_a, t_m, t_s, ω_1, ω_2) that need to be fitted. To ensure the model is differentiable at time t_s, the attenuation constant k is calculated as follows:

$$k = \frac{\omega_2}{\pi}\tan^{-1}\left(\frac{\pi}{\omega_2}(t_s - t_m)\right) \tag{8}$$

3.1.3. INA08 model

Inamdar et al. (2008) discovered that the hyperbolic function more accurately matches the observations during the nighttime decay of temperature. Consequently, the INA08 model replaces the exponential function with the hyperbolic function, as described below:

$$T_d(t) = T_0 + T_a\cos\left(\frac{\pi}{\omega}(t - t_m)\right), t < t_s \tag{9}$$

$$T_n(t) = (T_0 + \delta T) + \left[T_a\cos\left(\frac{\pi}{\omega}(t_s - t_m)\right) - \delta T\right]\frac{k}{(k + t - t_s)}, t \geq t_s \tag{10}$$

where all parameter definitions and the number of free parameters remain consistent with those of the GOT01 model.

3.1.4. GOT09 model

Starting from the energy balance equation of the surface, Göttsche and Olesen (2009) developed a novel DTC model that incorporates atmospheric attenuation of solar irradiation. By integrating total optical thickness, the new model better captures the morning rise of surface temperature and more accurately reflects the natural variability of DTC width and slope. The description of this new model is as follows:

$$T_d(t) = T_0 + T_a\frac{\cos(\theta_z)}{\cos(\theta_{z,\min})}e^{(m_{min} - m(\theta_z))\tau}, t < t_s \tag{11}$$

$$T_n(t) = (T_0 + \delta T) + \left[T_a\frac{\cos(\theta_{zs})}{\cos(\theta_{z,\min})}e^{(m_{\min} - m(\theta_{zs}))\tau} - \delta T\right]e^{\frac{-12}{\pi k}(\theta - \theta_s)}, t \geq t_s \tag{12}$$

where T_d, T_n, T_0, T_a, t_m, t_s, and δT hold the same definitions as in the GOT01 model, τ is the total optical thickness, θ is the thermal hour angle, θ_z is the thermal zenith angle, and m is the relative air mass. The values of θ, θ_z and m can be calculated by Iqbal (1983) and Vollmer and Gedzelman (2006). Additionally, the $\theta_{z,\min}$ is the minimum zenith angle when $\theta = 0$, $m_{\min}$ is the minimum relative air mass when $\theta_z = \theta_{z,\min}$, θ_s is the thermal hour angle when $t = t_s$, θ_{zs} is the thermal zenith angle obtained when $\theta = \theta_s$, R_M is the radius of Mars, and H is the scale height of the Martian atmosphere. Finally, the derivatives at $\theta = \theta_s$ lead to the calculation of k:

$$k = \frac{12}{\pi\dfrac{d\theta_z(\theta_s)}{d\theta}}\frac{\cos(\theta_{zs}) - \dfrac{\delta T}{T_a}\dfrac{\cos(\theta_{z,min})}{e^{\tau(m_{min} - m(\theta_{zs}))}}}{\sin(\theta_{zs}) + \tau\cos(\theta_{zs})\dfrac{\partial m(\theta_{zs})}{\partial\theta_z}} \tag{13}$$

Hence, in total, GOT09 involves six free parameters (i.e., T_0, T_a, t_m, t_s, δT, and τ).

3.1.5. DMT24 model

During the process of modeling surface temperatures on Mars, our observations indicate that the GOT09 model exhibits the most robust overall performance. However, we identified a potential opportunity for enhancing its accuracy during nighttime periods. Notably, previous studies, such as the INA08 model, have employed a hyperbolic function to represent nighttime temperature decay effectively. Motivated by this approach, we incorporated a similar function to refine the nighttime cooling component of the GOT09 model. This modification led to the development of the Diurnal Martian Temperature model (DMT24), which was described as follows:

$$T_d(t) = T_0 + T_a\frac{\cos(\theta_z)}{\cos(\theta_{z,\min})}e^{(m_{min} - m(\theta_z))\tau}, t < t_s \tag{14}$$

$$T_n(t) = (T_0 + \delta T) + \left[T_a\frac{\cos(\theta_{zs})}{\cos(\theta_{z,\min})}e^{(m_{\min} - m(\theta_{zs}))\tau} - \delta T\right]\frac{k}{\left(k + \dfrac{12}{\pi}(\theta - \theta_s)\right)}, t \geq t_s \tag{15}$$

where all parameter definitions and the number of free parameters remain consistent with those of the GOT09 model.

3.2. Parameter-reduction approaches

In order to apply the model with limited satellite mission and surface temperature data on Mars, it is essential to reduce the number of free parameters. Previous studies have suggested various PRAs. For example, the day-to-day change in residual temperature can approximate zero (Schädlich et al., 2001). Additionally, the time when free attenuation begins can be estimated to be about 1 h before sunset (Duan et al., 2014). In this study, we applied the most used PRAs in previous research to all the models in section 3.1. Two main PRAs are used: (1)setting δT to zero, (2) setting t_s to 1 h before the sunset time (t_{ss}). In the case of VAN06 and GOT09, which involve six parameters, two additional PRAs are applied to fix ω_1, ω_2, and τ. In total, there are twelve four-parameter DTC models after applying these PRAs. Detailed information about these models is provided in Table 2.

3.3. Solutions

Levenberg-Marquardt algorithm is employed to fit the parameters of

Table 2
General information of the four-parameter DTC models.

Model name	Parameters	PRAs
GOT01_dT	T_0, T_a, t_m, t_s, δT	$\delta T = 0$
GOT01_ts	T_0, T_a, t_m, t_s, δT	$t_s = t_{ss} - 1$
VAN06_ts_w1	T_0, T_a, t_m, t_s, ω_1, ω_2	$t_s = t_{ss} - 1$; $\omega_1 = DD$
VAN06_ts_w2	T_0, T_a, t_m, t_s, ω_1, ω_2	$t_s = t_{ss} - 1$; $\omega_2 = DD$
INA08_dT	T_0, T_a, t_m, t_s, δT	$\delta T = 0$
INA08_ts	T_0, T_a, t_m, t_s, δT	$t_s = t_{ss} - 1$
GOT09_dT_tau	T_0, T_a, t_m, t_s, δT, τ	$\delta T = 0$; $\tau = 0.01$
GOT09_dT_ts	T_0, T_a, t_m, t_s, δT, τ	$\delta T = 0$; $t_s = t_{ss} - 1$
GOT09_ts_tau	T_0, T_a, t_m, t_s, δT, τ	$t_s = t_{ss} - 1$; $\tau = 0.01$
DMT24_dT_tau	T_0, T_a, t_m, t_s, δT, τ	$\delta T = 0$; $\tau = 0.01$
DMT24_dT_ts	T_0, T_a, t_m, t_s, δT, τ	$\delta T = 0$; $t_s = t_{ss} - 1$
DMT24_ts_tau	T_0, T_a, t_m, t_s, δT, τ	$t_s = t_{ss} - 1$; $\tau = 0.01$

Table 3
Initial values of the free parameters for the DTC models.

Model name	T_0	T_a	t_m	t_s	δT	ω_1	ω_2	τ
GOT01	T_{min}	$T_{max} - T_{min}$	13	$t_{ss} - 1$	0	–	–	–
VAN06	T_{min}	$T_{max} - T_{min}$	13	$t_{ss} - 1$	–	12	12	–
INA08	T_{min}	$T_{max} - T_{min}$	13	$t_{ss} - 1$	0	–	–	–
GOT09	T_{min}	$T_{max} - T_{min}$	13	$t_{ss} - 1$	0	–	–	0
DMT24	T_{min}	$T_{max} - T_{min}$	13	$t_{ss} - 1$	0	–	–	0
GOT01_dT	T_{min}	$T_{max} - T_{min}$	13	$t_{ss} - 1$	–	–	–	–
GOT01_ts	T_{min}	$T_{max} - T_{min}$	13	–	0	–	–	–
VAN06_ts_w1	T_{min}	$T_{max} - T_{min}$	13	–	–	–	DD	–
VAN06_ts_w2	T_{min}	$T_{max} - T_{min}$	13	–	–	DD	–	–
INA08_dT	T_{min}	$T_{max} - T_{min}$	13	$t_{ss} - 1$	0	–	–	–
INA08_ts	T_{min}	$T_{max} - T_{min}$	13	–	0	–	–	–
GOT09_dT_tau	T_{min}	$T_{max} - T_{min}$	13	$t_{ss} - 1$	–	–	–	–
GOT09_dT_ts	T_{min}	$T_{max} - T_{min}$	13	–	–	–	–	0.01
GOT09_ts_tau	T_{min}	$T_{max} - T_{min}$	13	–	0	–	–	–
DMT24_dT_tau	T_{min}	$T_{max} - T_{min}$	13	$t_{ss} - 1$	–	–	–	–
DMT24_dT_ts	T_{min}	$T_{max} - T_{min}$	13	–	–	–	–	0.01
DMT24_ts_tau	T_{min}	$T_{max} - T_{min}$	13	–	0	–	–	–

*Tmin and Tmax represent the minimum and maximum of input temperatures, respectively.

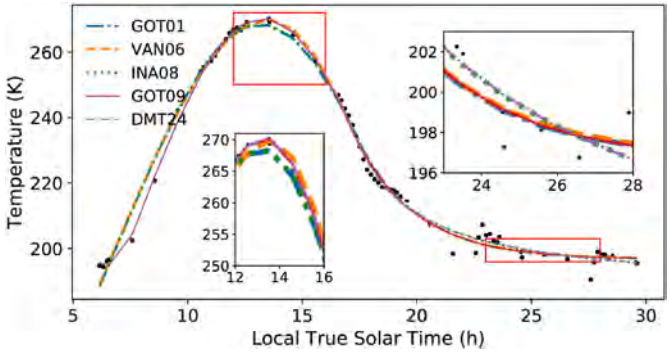

Fig. 1. Martian surface temperature observed by Curiosity observations at sol 3330 (black dots), and its diurnal variation reconstructed by DTC models (colored lines).

DTC models. The initial values of free parameters for each DTC are listed in Table 3.

4. Results and analysis

4.1. Performance of DTC models with in-situ data

An example of DTC models on Mars is provided in Fig. 1 to illustrate a typical DTC observed by Curiosity MSL, aiding in a clearer understanding of the variations between models. All five DTC models effectively replicate the diurnal cycle of surface temperature on Mars. The GOT01, VAN06, and INA08 models exhibit nearly identical predictions around sunrise, with the primary distinction being noticeable in the case of the GOT09 model during this period. The GOT09 model captures a smooth and gradual increase in Martian surface temperature around sunrise, aligning closely with findings conducted on Earth (Göttsche and Olesen, 2009). At noon, VAN06 diverges from GOT01 and INA08, as it employs a distinct ω for the cosine term. After sunset, the INA08 model starts to demonstrate differences with the GOT01, VAN06, and GOT09 models because of the hyperbolic function it employs. The DMT24 model is a refined iteration of the GOT09 model, integrating a hyperbolic function to characterize the nocturnal temperature reduction. This selection stems from the hyperbolic function's superior alignment with observations on Mars.

The comparison between surface temperatures obtained from in-situ measurements and those reconstructed by five DTC models is depicted in Fig. 2. It shows the efficacy and overall accuracy of these models in different missions. For Viking1, both the GOT09 and DMT24 models exhibit a distribution that is more centered around the identity line, suggesting greater accuracy in their modeling results. The remaining three models (i.e. GOT01, VAN06, INA08) exhibit analogous error distributions, each manifesting notable biases in proximity to temperatures around 210K. This bias primarily stems from the falsely sharp increase in surface temperature around sunrise. The outcomes for Insight, Perseverance, and Curiosity closely resemble those observed in Viking1 regarding error distributions. While the root mean square error (RMSE) values vary across different missions, the DMT24 model consistently surpasses the other four models, demonstrating the lowest RMSE and presenting a reduction in RMSE ranging from 4.48 % to 21.9 % compared to the GOT09 model (except Viking1). Following closely in second place is the GOT09 model, trailed by the INA08, VAN06, and GOT01 models.

Fig. 3 presents the bias of five DTC models binned according to local time and solar longitude. In Viking1 observations, both GOT09 and DMT24 models exhibit minimal bias, underscoring their clear superiority compared to the other three models. In Insight observations, GOT01, VAN06, and INA08 models display substantial bias during sunrise, particularly from 5:00 to 9:00, where they demonstrate a notable positive-negative-positive bias pattern. In contrast, both GOT09 and DMT24 models show relatively smaller biases compared to the others. Nevertheless, all five models exhibit a strong positive bias during the early night (before 21:00 local time) and transition to a negative bias from late night to before sunrise (22:00–3:00). Regarding Perseverance and Curiosity, their bias distributions mirror those from Insight observations but with smaller magnitudes. Furthermore, the pronounced bias during sunrise for GOT01, VAN06, and INA08 models in Curiosity's case suggests a significant orbital season variation.

The frequency distribution of RMSE values within each 0.5 K interval illustrates the daily performance of these models (Fig. 4). For Viking1, the RMSEs of the GOT01, VAN06, and INA08 models mostly range from 1 to 3K, while those of the GOT09 and DMT24 models are mostly in the range of 0.5–1K. Regarding Insight and Perseverance, most RMSEs of the GOT01, VAN06, and INA08 models fall in the range of 1–2K, with the INA08 model slightly outperforming the others. The majority of results from the DMT24 model show RMSEs ranging from 0.5 to 1.5K for Insight and 0.5–1K for Perseverance, showing an improvement of about 0.5K compared to the GOT09 model. In the case of Curiosity, the RMSEs are notably larger than in other missions, mostly ranging from 1 to 3K. This discrepancy may stem from a diminished precision in Curiosity's measurement of nighttime low temperatures. Nonetheless, it is worth noting that the DMT24 model demonstrates a notably higher frequency of lower RMSEs within the range of 0.5–1.5K compared to other models.

Fig. 5 illustrates the hourly RMSEs of DTC models, computed based on averages over sols binned from all available data. Large RMSE values are observed to be more prevalent during nocturnal periods and around sunrise. The RMSE values from various in-situ data sources remain relatively consistent around sunrise, hovering at approximately 4K for the GOT01, VAN06, and INA08 models, and within a 2K range for the GOT09 and DMT24 models. The sunrise time can be roughly estimated by observing the rapid increase in RMSE around 6:00. RMSEs peak shortly after sunrise within approximately 2 h, then gradually decreasing. However, there is another increase in RMSE after sunset. When assessing the performance of various DTC models, distinct performance patterns emerge over different times of the day. Specifically, the GOT09 and DMT24 models demonstrate minimal errors around sunrise, while the VAN06 model exhibits its superior performance during afternoons. The INA08 and DMT24 models display diminished errors during nighttime. These advancements align with their respective developments derived from the GOT01 model.

In Fig. 6, we further assess the overall and seasonal performance of the five DTC models. Among them, the DMT24 model consistently outperforms the other models across all missions. Regarding performance across different seasons, DMT24 model exhibits lower RMSE

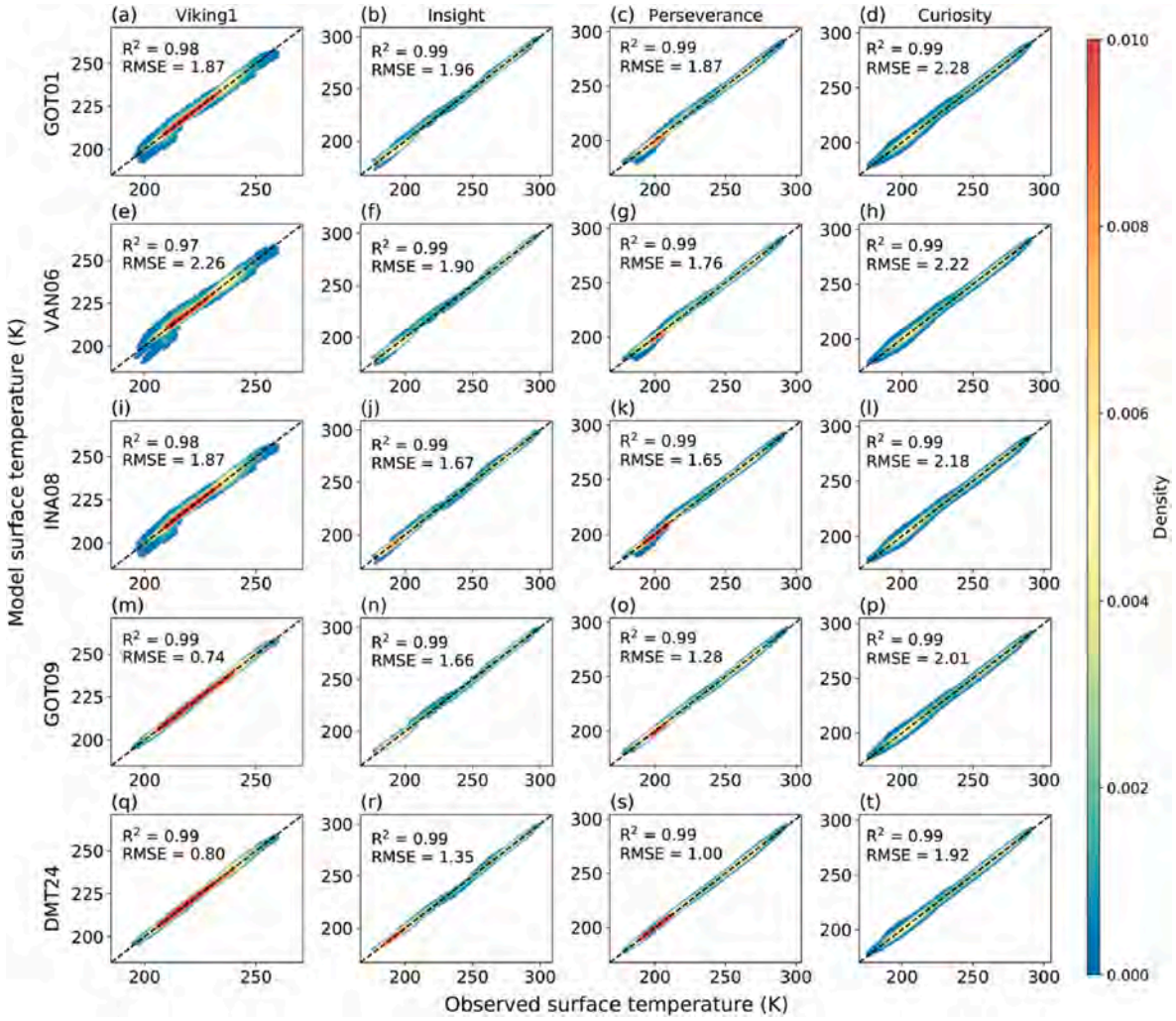

Fig. 2. Scatter density plots of Martian surface temperature observed by in situ rovers and those reconstructed by GOT01 (a–d), VAN06 (e–h), INA08 (i–l), GOT09 (m–p), and DMT24 (q–t). The columns from left to right represent data from Viking1, Insight, Perseverance and Curiosity observations.

values during the perihelion season. This trend can be attributed to the increased occurrence of local or global dust storms during these periods. Dust plays a significant role in reducing the range of diurnal surface temperatures by lowering daytime temperatures and elevating nighttime temperatures (Wilson and Smith, 2006). The performance of the GOT01, VAN06, and INA08 models exhibits variability across distinct missions. Specifically, the INA08 model outperforms the VAN06 model on the Perseverance and Insight datasets, and the VAN06 model outperforms the GOT01 model on the same datasets. Conversely, in the analysis of Viking1 data, the GOT01 model surpasses the VAN06 model, exhibiting only marginal deviations from the performance of the INA08 model.

4.2. Parameter characteristics

While the GOT01, VAN06, INA08, GOT09, and DMT24 models all share parameters such as T_0, T_a, t_m, t_s, and δT (excluding VAN06), their values may vary significantly when modeling a same day. Therefore, it is crucial to thoroughly understand their individual characteristics. This understanding could aid in deducing surface thermal properties, identifying surface freeze/thaw status, and optimizing parameters in satellite applications.

Fig. 7 illustrates the distribution of parameters across different models and missions. Regarding T_0, it is noteworthy that the T_0 value in the VAN06 model is smaller than in the other four models. Additionally, the T_0 values in the GOT01 and INA08 models are similar, as are those in the GOT09 and DMT24 models, suggesting that T_0 is primarily influenced by daytime temperature observations. Conversely, T_a exhibits the opposite trend compared to T_0. Specifically, the T_a values in the VAN06 model are larger than in the other four models. Moreover, the T_a values in the GOT01 and INA08 models are comparable, as are those in the GOT09 and DMT24 models. This disparity arises because the daily maximum temperature is the sum of T_0 and T_a. In terms of t_m, the distribution in the VAN06 model deviates from that of the other four models, which share a similar distribution. This discrepancy stems from the fact that in these four models, t_m directly indicates the time when the temperature reaches its maximum, whereas in the VAN06 model, it determines the usage of either ω_1 or ω_1. For t_s, all five models exhibit a similar distribution (except for Viking1), suggesting a commonality in t_s across these models. Regarding δT, the distributions of GOT01 and GOT09 are similar, as are those of INA08 and DMT24, a consequence directly attributed to the models' decay functions.

Fig. 8 shows the annual variation of parameters observed by the Curiosity rover, serving as an exemplary demonstration. In regard to T_0, discernible seasonal fluctuations are apparent. These fluctuations mirror the changes in radiation received by the Martian surface, wherein radiation decreases from Ls 0–90° (aphelion season) and increases thereafter. During perihelion season, T_0 remains relatively stable, attributed to the dust effect, which hinders radiation from reaching the Martian surface. Similarly, T_a exhibits consistent variation across seasons and is

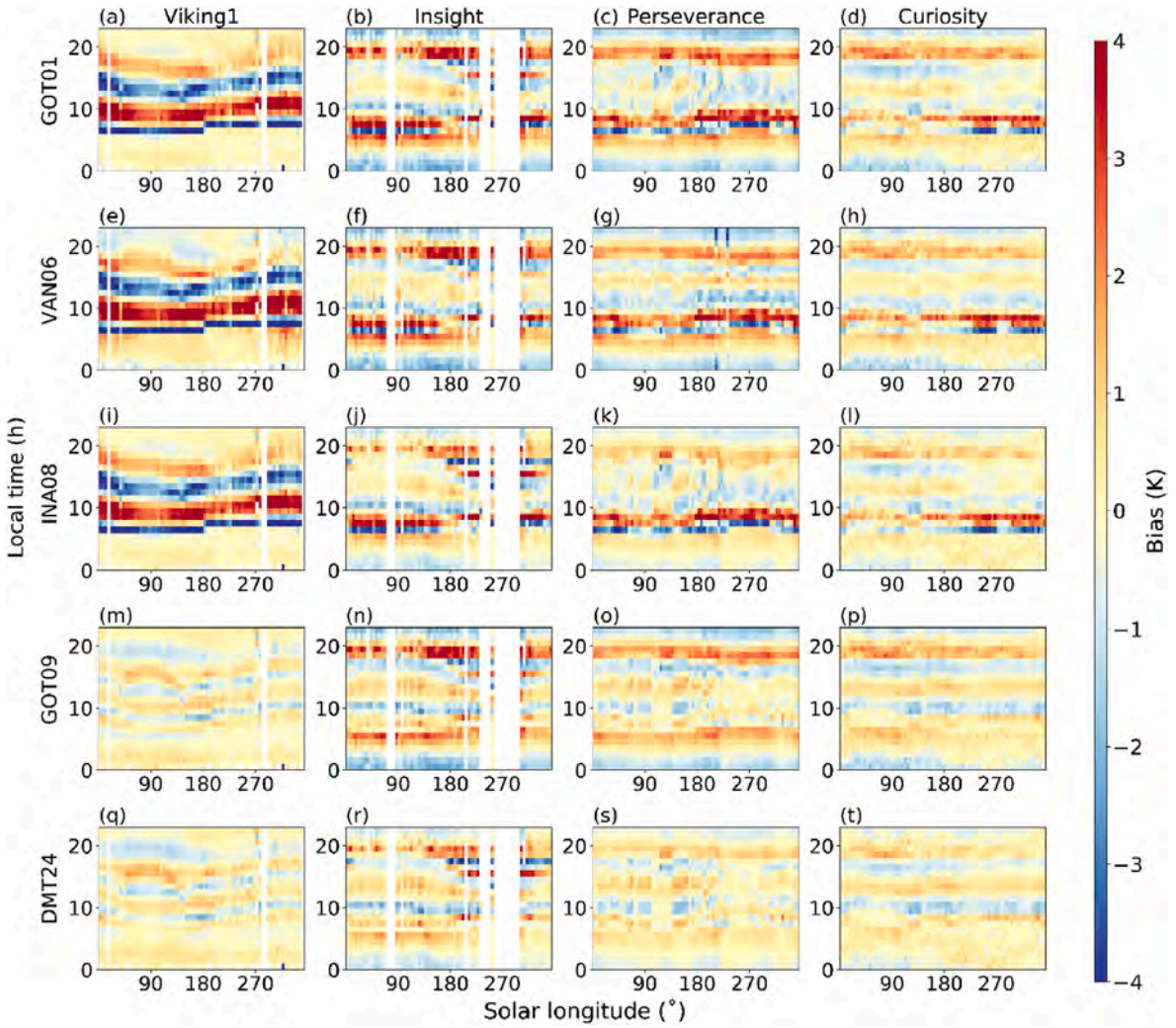

Fig. 3. Bias of GOT01 (a–d), VAN06 (e–h), INA08 (i–l), GOT09 (m–p), and DMT24 models(q-t) in the (local time, solar longitude) bins. The columns from left to right represent data from Viking1, Insight, Perseverance and Curiosity.

more sensitive to the influence of dust particles. Regarding t_m, measurements from GOT01, INA08, GOT09, and DMT24 closely align, remaining relatively stable around 13:20. However, t_m from VAN06 varies considerably, spanning from 13:00 to 14:00. As for t_s, a consistent trend of change is observed across models. Specifically, t_s increases from Ls 0–100°, decreases from Ls 100–230°, and then stabilizes during Ls 270–360°. δT from GOT01 and GOT09 demonstrates relatively stable values around −15K, whereas δT from INA08 and DMT24 exhibits obvious seasonal variations, following similar trends with t_s. In terms of τ, it displays small values in the aphelion season and relatively larger values in the perihelion season, corresponding to the climatology of dust on Mars. Overall, the variations in parameters are largely dependent on orbital season, prompting further evaluation of these variations with respect to the distance from the sun to Mars (Fig. 9). Parameters that are highly dependent on orbital season, such as T_0, T_a, t_s, and δT (only for INA08 and DMT24), remain stable when the distance is small. However, they show strong linear trends when the distance exceeds 1.45 AU. Additionally, τ exhibits relatively large values when the distance is within 1.45 AU, corresponding to increased dust during Martian perihelion season.

4.3. Performance of DTC models with satellite data

Increasing the number of parameters in DTC models, along with a larger volume of data during the fitting process, generally leads to better performance. However, a primary application of DTC models is in reconstructing diurnal temperature variations, especially when observations are scarce. Therefore, it is imperative to assess the performance of DTC models based on satellite data. To simulate common conditions with data gathered from two polar satellites, we streamline the parameters of DTC models to four. Additionally, we select observations closest to 3:00 and 15:00 (corresponding to MCS overpass times) and those near 6:00 and 18:00 (corresponding to THEMIS overpass times) as inputs. The hourly RMSEs of the four-parameter DTC models fitted with four inputs are illustrated in Fig. 10. Overall, errors notably increase as parameters and observations decrease. The significant decline in model performance observed between 7:00 and 14:00 can be partly attributed to the absence of observations around these times. Additionally, since surface temperatures typically peak around noon, accurately fitting temperature amplitude becomes challenging without the maximum surface temperature data. Nevertheless, some unexpected consistent outcomes emerge. Specifically, the PRA "$t_s = t_{ss} - 1$" consistently outperforms the PRA "$\delta T = 0$" across four in-situ datasets. Additionally, the VAN06_ts_w2 model exhibits superior performance compared to the VAN06_ts_w1 model. To provide a more intuitive representation of the models' performance, we rank these twelve models based on their mean errors in Table 4. The INA08_ts model ranks first among the twelve models, exhibiting a mean RMSE of 3.15K. It is succeeded by the DMT24_ts_tau, GOT01_ts, VAN06_ts_w2, and GOT09_ts_tau models, which demonstrate RMSE values ranging from 3.29 to 3.77K.

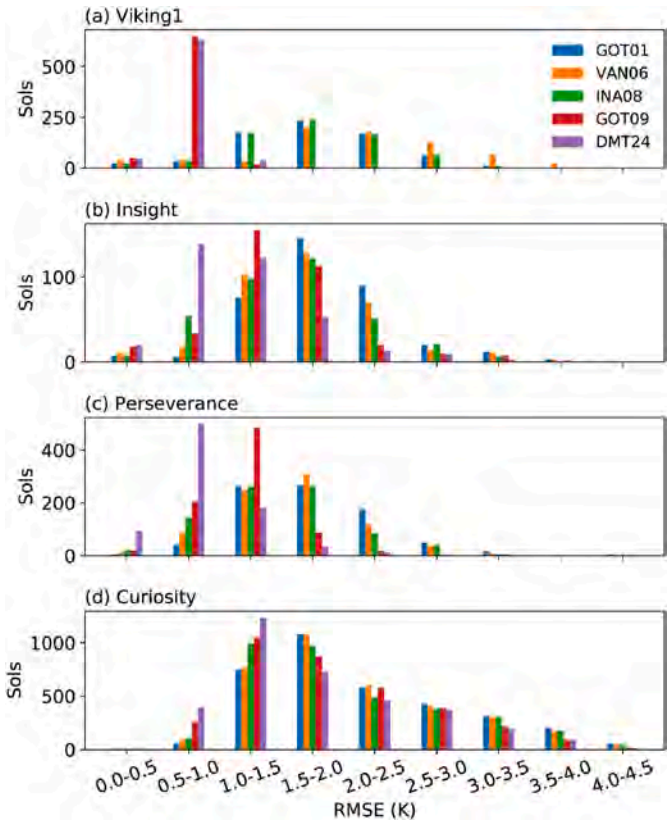

Fig. 4. Histograms of the daily RMSE of DTC models for (a) Viking1, (b) Insight, (c) Perseverance and (d) Curiosity observations.

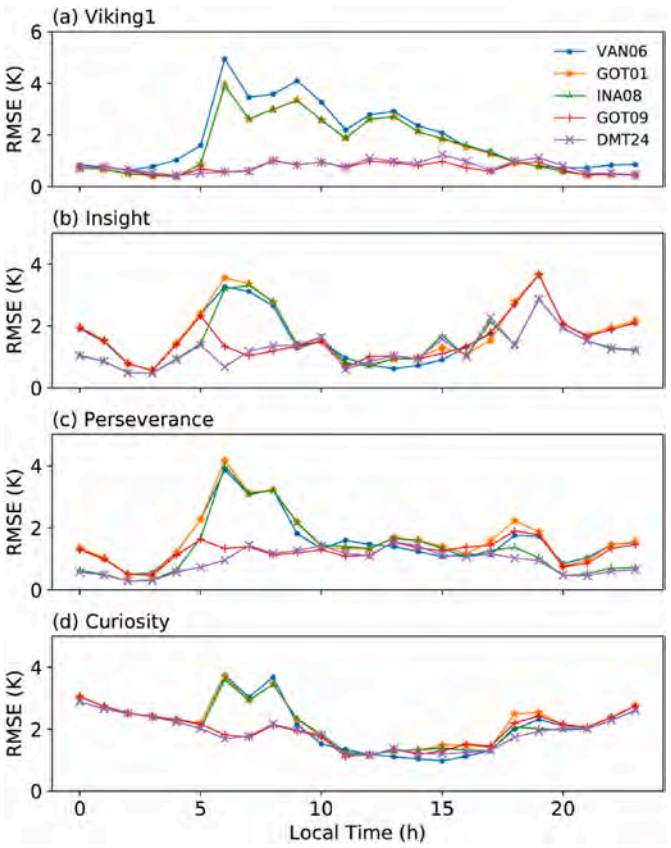

Fig. 5. Averaged hourly RMSE of DTC model for (a) Viking1, (b) Insight, (c) Perseverance, and (d) Curiosity observations.

Fig. 11 displays two examples in describing the diurnal variation of Martian surface temperature derived from satellite data, showcasing the efficacy of DTC modes applied to satellite observations. INA08_ts was deliberately chosen because of its consistent superior performance. The validation process relies on data from the Perseverance mission. Our selection criteria for satellite observations encompassed spatial proximity of within 3° in latitude and longitude of the Perseverance rover, as well as temporal discrepancies within 5 degrees of solar longitude (Ls), considering the limited data available. The 5-degree difference in Ls is unlikely to significantly affect the accuracy because the diurnal temperature cycles change very little on consecutive sols (Munguira et al., 2023). On Perseverance sol 307, a systematic bias existed between the temperatures constructed by satellite data and in-situ measurements, with the satellite observations consistently smaller than the in-situ data. This bias resulted in an overall RMSE of 6.10 K between the in-situ data and the temperatures reconstructed by satellite. On sol 422, the INA08_ts model exhibited a significant underestimation in both temperature amplitude and nighttime temperature, resulting in an overall RMSE of 4.67 K. These discrepancies primarily stem from observations near 3:00 and 15:00. Consequently, the accuracy of surface temperature reconstruction heavily depends on the quality of satellite observations. However, discrepancies between satellite and in-situ observations are inevitable due to inconsistent scales. Several factors, such as the approximation of actual locations, temperature estimates for adjacent days, and the rapid estimation of surface temperature retrieved by THEMIS, may influence these discrepancies. The combination of these factors can exacerbate nonlinear errors. Therefore, it is crucial to carefully consider these possible factors in practical satellite applications.

5. Discussion

Dust events are the most frequent and significant weather phenomena on Mars, making a profound impact on the planet's surface temperature by altering radiance received by ground. Thus, we proceed to conduct an additional assessment of these models' performance specifically on days characterized by dust presence. Table 5 displays the accuracy of DTC models on clear days and dust days, as observed by Curiosity. Dusty days are defined as those where the optical depth at 880 nm exceeds 1. The GOT01, VAN06, and INA08 models exhibit higher RMSE values on dust days compared to clear days. Conversely, the GOT09 and DMT24 models demonstrate lower RMSE values on dust days than on clear days. The GOT09 and DMT24 model outperforms others because of their incorporation of a parameter for total optical thickness. This feature is particularly beneficial for modeling the Martian atmosphere given the prevalence of local and global dust storms. However, setting it as a constant to create four-parameter DTC models in Section 4.3 may seem somewhat arbitrary. Therefore, there is a critical necessity to explore more robust PRAs for these two models. Fortunately, we have identified a strong correlation between the total optical thickness estimated by the GOT09 and DMT24 model and the visual opacity of the Martian sky (Lemmon, 2023) during the 2018 Mars global dust storm (Fig. 12). This correlation suggests a new potential PRA for these two models by integrating opacity data from additional sources to refine the estimation of total optical thickness. Moreover, surface temperatures largely depend on surface albedo and thermal inertia values (Piqueux et al., 2023). Therefore, information about surface properties can be invaluable for DTC modeling, especially when there are limited diurnal thermal observations available.

Due to Mars' thin and tenuous atmosphere, surface temperatures primarily respond to variations in solar irradiation over diurnal and seasonal cycles. However, temperature fluctuations are also influenced

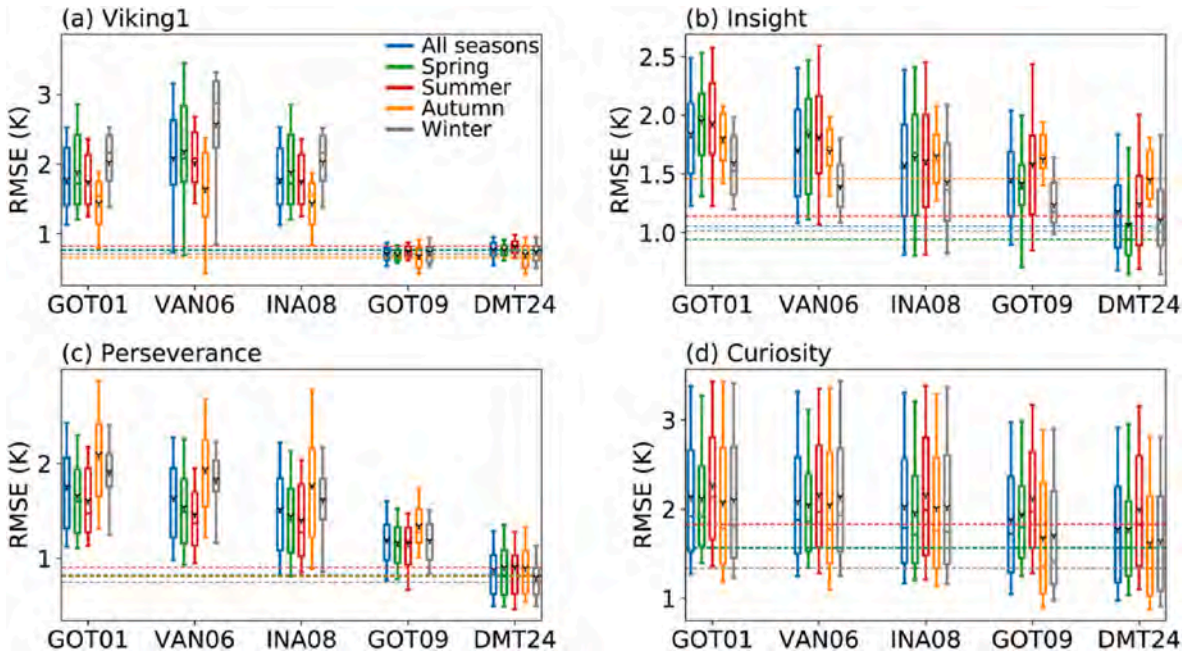

Fig. 6. Boxplots of overall and seasonal RMSE of DTC models for (a) Viking1, (b) Insight, (c) Perseverance, (d) Curiosity observations. The top and bottom of the box are the first quartile and the third quartile of the RMSEs, respectively. The whiskers extend to the farthest data point lying within 1.5 times the inter-quartile range from the box. The band and point inside the box denote the median and mean RMSE for each model, respectively. Dashed lines show the median RMSEs for DMT24 models as baseline references.

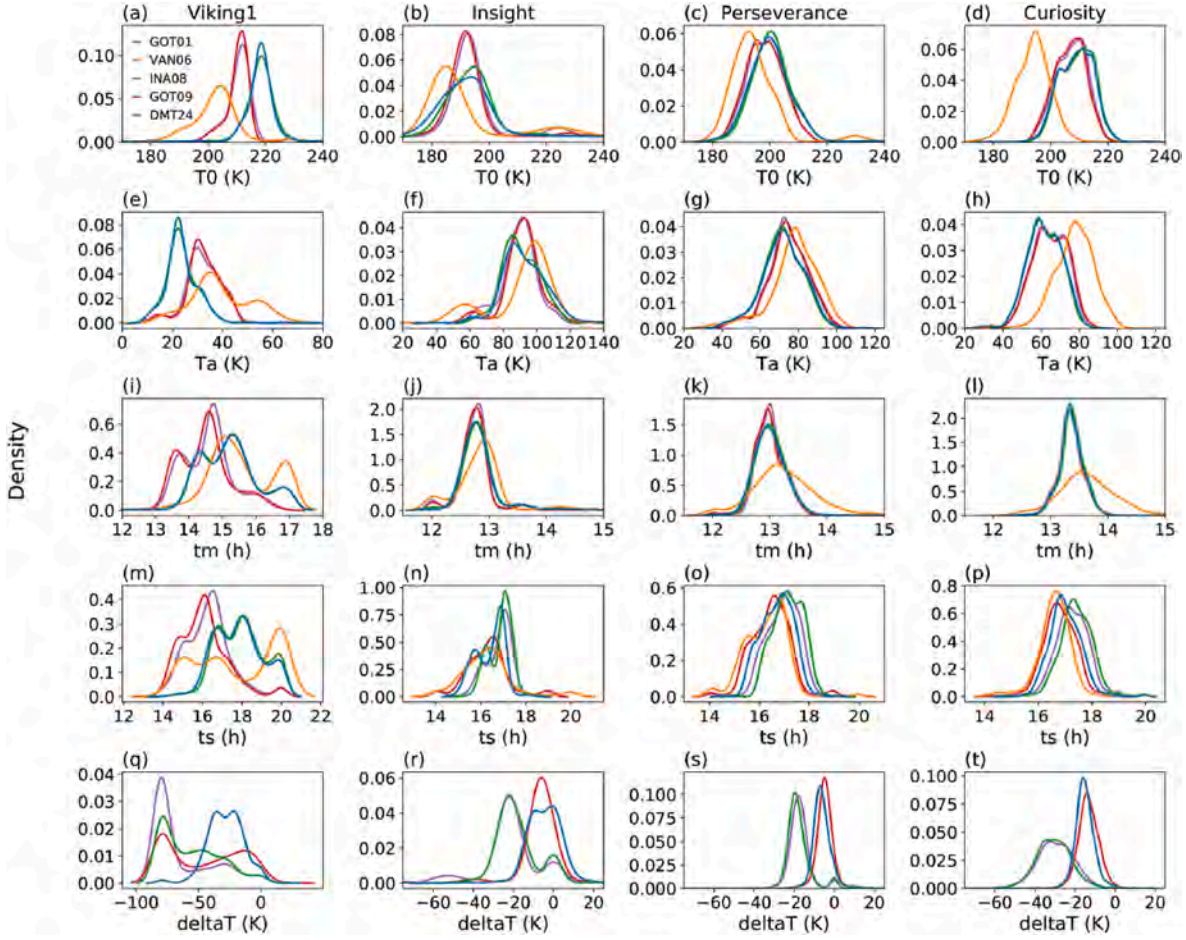

Fig. 7. Density distributions of parameters in DTC models from (a) Viking1, (b) Insight, (c) Perseverance, (d) Curiosity observations.

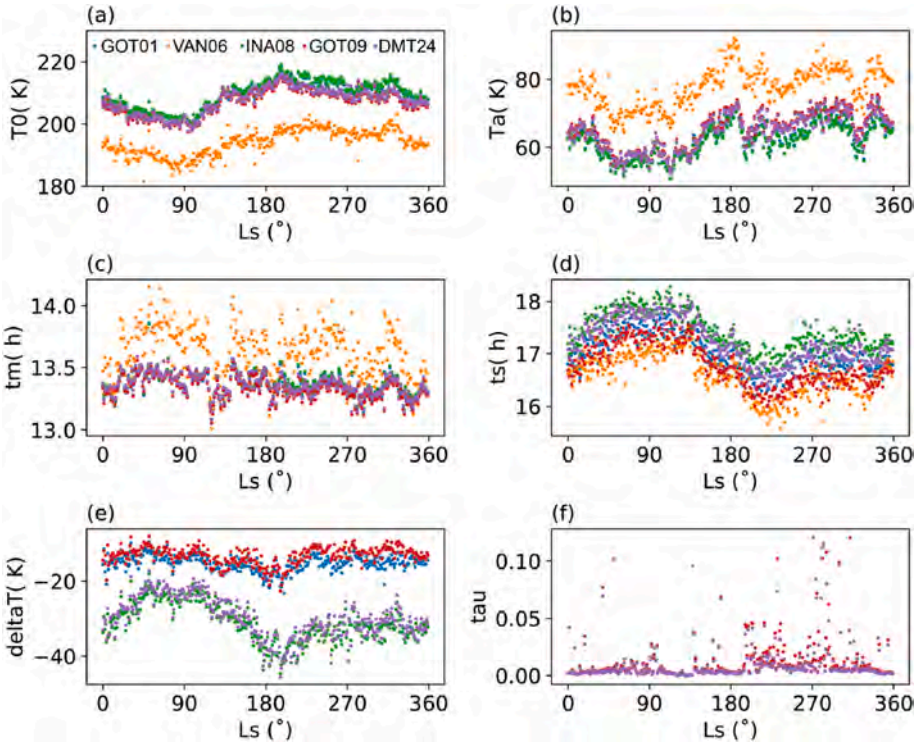

Fig. 8. Seasonal variations of parameters (a) T_0, (b) T_a, (c) T_m, (d) t_s, (e) δT, and (f) τ derived from Curiosity observations.

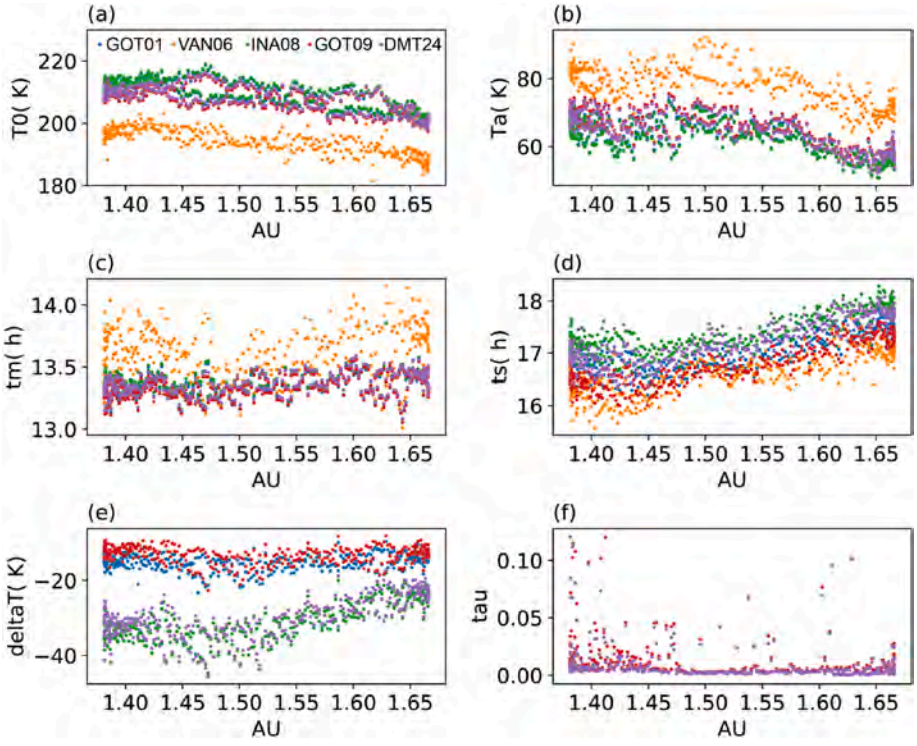

Fig. 9. Variations of parameters (a) T_0, (b) T_a, (c) t_m, (d) t_s, (e) δT, and (f) τ, against the distance from Sun to Mars derived from Curiosity observations.

by several localized factors. On regional and local scales, surface temperature dynamics are affected by properties such as surface albedo, thermal inertia, atmospheric opacity, and the slope and shadowing effects of the terrain. As a result, the parameters used in DTC models can be interpreted in terms of the thermophysical properties of the surface and atmosphere. In particular, seasonal variations in the parameters T_a and T_0 correspond to seasonal changes in solar irradiation. The timing of sunrise and the distribution of sunlight throughout the day are also strongly influenced by these seasonal variations, affecting the parameters t_m, ω, t_s. On a more localized scale, T_0 is primarily determined by surface albedo, as higher albedo reflects more sunlight, reducing heat absorption. Meanwhile, T_a is closely linked to thermal inertia, with

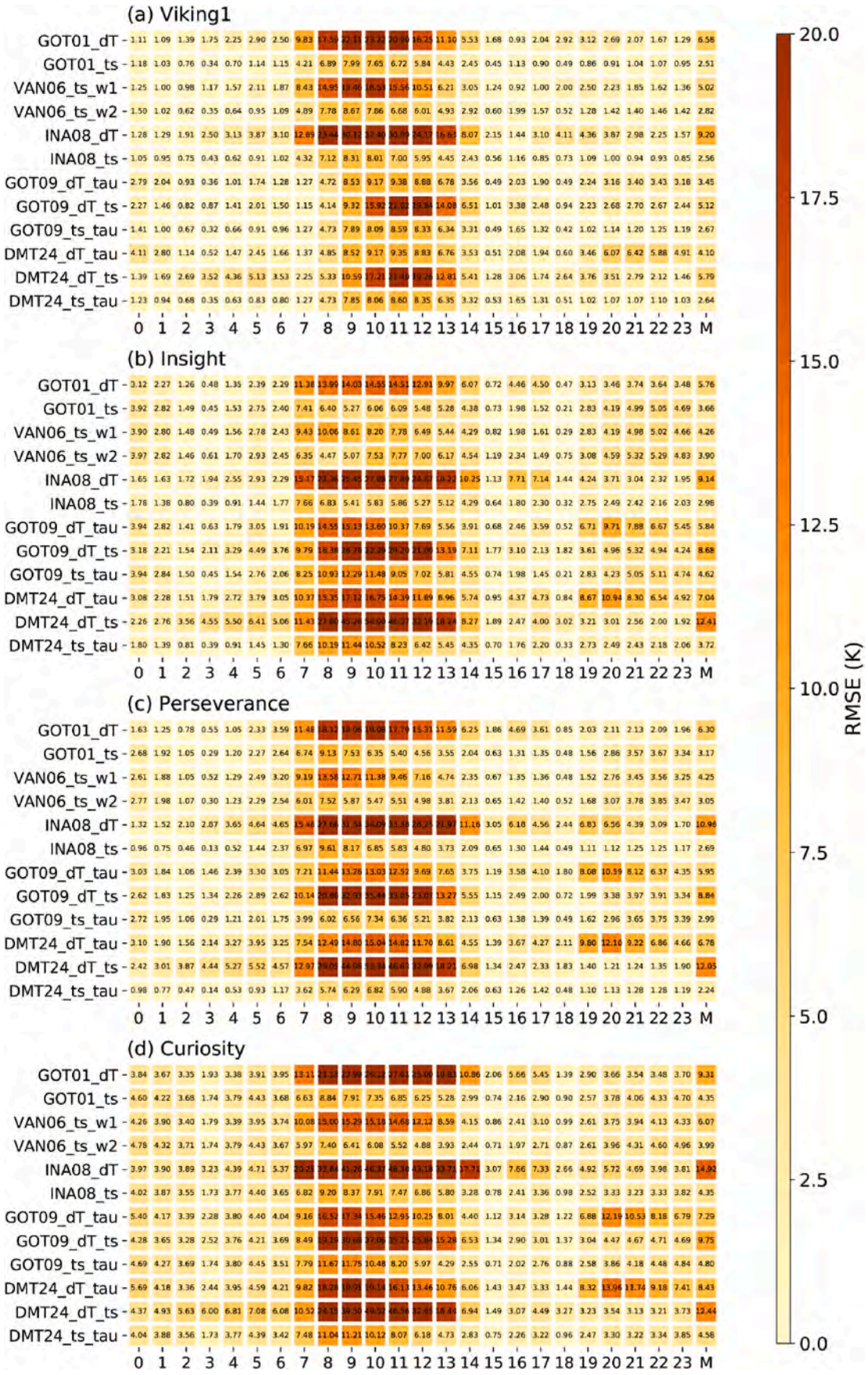

Fig. 10. Averaged hourly RMSE of four-parameter DTC models for (a) Viking1, (b) Insight, (c) Perseverance, (d) Curiosity observations.

Table 4
Ranking order of performance for four-parameter DTC models.

Model name	Rank	Mean RMSE (K)
GOT01_dT	9	6.99
GOT01_ts	3	3.42
VAN06_ts_w1	6	4.90
VAN06_ts_w2	4	3.44
INA08_dT	12	11.05
INA08_ts	1	3.15
GOT09_dT_tau	7	5.63
GOT09_dT_ts	10	8.09
GOT09_ts_tau	5	3.77
DMT24_dT_tau	8	6.59
DMT24_dT_ts	11	10.67
DMT24_ts_tau	2	3.29

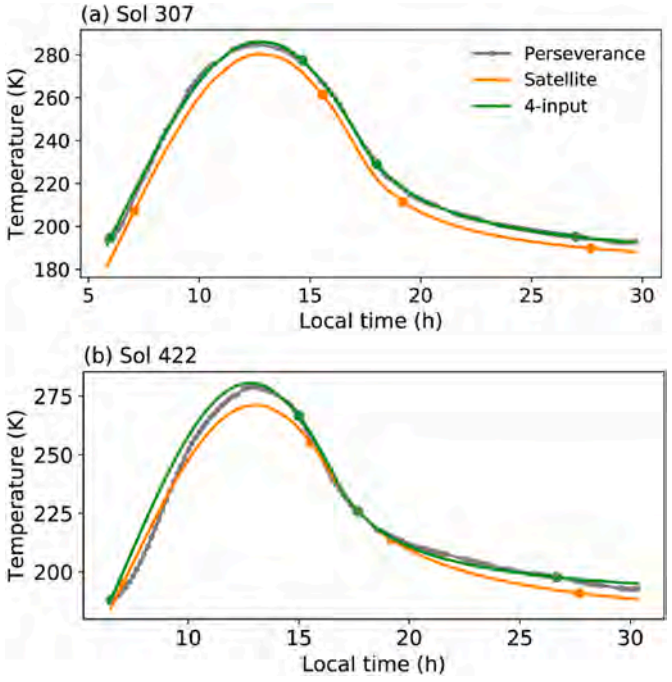

Fig. 11. DTC estimated by the INA08_ts model driven by the Perseverance and satellite observations at (a) sol 307 and (b) sol 422. Solid lines represent the constructed temperatures, dots denote the input observations.

Table 5
Mean RMSE (unit: K) of DTC models in clear days and dust days.

	GOT01	VAN06	INA08	GOT09	DMT24
Clear days	2.14	2.08	2.03	1.88	1.77
Dust days	2.22	2.24	2.15	1.74	1.67

materials of high thermal inertia retaining heat longer and cooling more gradually overnight. Another crucial factor is τ, which represents the degree to which the atmosphere scatters and absorbs sunlight. It plays a particularly significant role in Mars' dust-laden atmosphere, moderating the rate of temperature increase after sunrise and influencing the overall thermal behavior of the surface.

Our assessment on Mars indicates that DTC models perform effectively regardless of clear-sky conditions, owing to the Martian tenuous atmosphere. However, our study has several potential uncertainties and limitations that warrant further investigation in future studies. One notable limitation is that the selected rovers primarily operate near the equator and in low latitudes due to the constraints of landers. Further investigation is needed to assess the accuracy of DTC models in middle and higher latitudes, particularly with continuous, high-quality

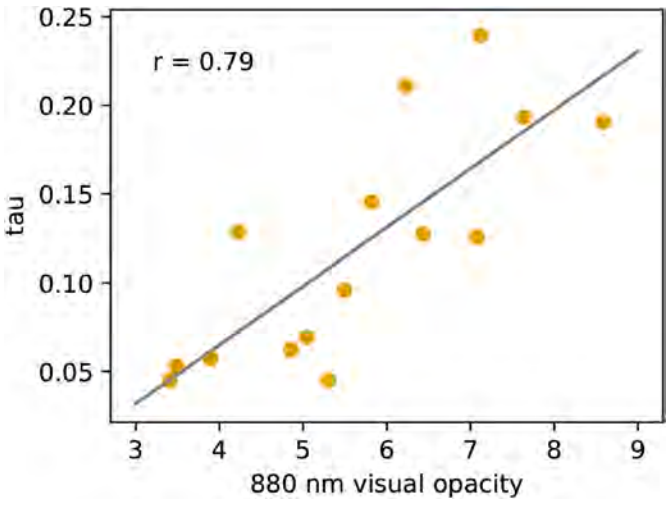

Fig. 12. Scatter plot of 880 nm visual opacity observed by Curiosity and τ estimated by DMT24 model. The solid line represents the linear regression of the observed opacity and estimated τ.

observations in those regions in the future. Additionally, understanding the parameter characteristics in middle and higher latitudes is crucial. These characteristics can be leveraged to examine the global applicability of PRAs.

6. Conclusions

In this study, we constructed and assessed the DTC models on Mars surface using in-situ datasets from the Viking, Insight, Perseverance, and Curiosity rovers. These models effectively replicate the diurnal variations of surface temperatures on Mars with an overall error from 0.74 to 2.28 K. The most notable RMSEs predominantly occur during nighttime or around sunrise. Among the models, DMT24 exhibits the superior overall performance, primarily attributed to accurately reproduce the slow and smooth increase of Martian surface temperatures around sunrise, as well as its strong performance during nighttime. This improvement stems largely from the use of a hyperbolic function to describe nighttime cooling with capturing temperature variations more accurately than the GOT09 model. Model performance varies across different sites and seasons. Models incorporating parameters for optical thickness (i.e. GOT09 and DMT24) consistently show smaller errors during the perihelion season compared to the aphelion season due to increased dust storms during the former period.

In regard to the distribution of parameters, those from VAN06 differ significantly from the other models. The remaining four models exhibit similar parameter distributions, except for δT. GOT01 and GOT09 show a similar distribution for δT, whereas INA08 and DMT24 display a comparable distribution. These parameters demonstrate strong seasonal variations, which are highly correlated with the distance between Mars and the Sun.

The performance of DTC models is further evaluated by satellite data through PRAs with considering the inherent limitations in observations from Mars. Overall, the PRA "$t_s = t_{ss} - 1$" outperforms the PRA "$\delta T = 0$". The INA08_ts model consistently outperforms all other models, followed by DMT24_ts_tau, GOT01_ts, VAN06_ts_w2, and GOT09_ts_tau models. However, there is not much disparity between these best models in each type of DTC model, as their performance relies heavily on the quantity of observations. Furthermore, the effectiveness of DTC models in satellite applications is exemplified. It is worth noting that the quality of observations can significantly impact the temperature outcomes.

CRediT authorship contribution statement

Yu Wang: Writing – original draft, Visualization, Investigation, Data curation, Conceptualization. **Shuanggen Jin:** Writing – review & editing, Supervision, Funding acquisition.

Data availability statement

The calibrated Mars surface temperature data used in this study are all available via the NASA Planetary Data System (PDS).

Declaration of competing interest

All authors disclosed no financial and personal relationships with other people or organizations.

Acknowledgments

This study was supported by the National Key Research and Development Program (Grant No. 2021YFA0716100): Exploration of habitable environments and biosignatures on Mars, China.

Data availability

The calibrated Mars surface temperature data used in this study are all available via the NASA Planetary Data System (PDS).

References

Arnold, N.S., Butcher, F.E.G., Conway, S.J., Gallagher, C., Balme, M.R., 2022. Surface topographic impact of subglacial water beneath the south polar ice cap of Mars. Nat. Astron. 6, 1256–1262. https://doi.org/10.1038/s41550-022-01782-0.

Atri, D., Abdelmoneim, N., Dhuri, D.B., Simoni, M., 2023. Diurnal variation of the surface temperature of mars with the emirates mars mission: a comparison with curiosity and perseverance rover measurements. Mon. Not. R. Astron. Soc. Lett. 518, L1–L6. https://doi.org/10.1093/mnrasl/slac094.

Bandfield, J.L., 2007. High-resolution subsurface water-ice distributions on Mars. Nature 447, 64–67. https://doi.org/10.1038/nature05781.

Banerdt, W.B., Smrekar, S.E., Banfield, D., Giardini, D., Golombek, M., Johnson, C.L., Lognonné, P., Spiga, A., Spohn, T., Perrin, C., Stähler, S.C., Antonangeli, D., Asmar, S., Beghein, C., Bowles, N., Bozdag, E., Chi, P., Christensen, U., Clinton, J., Collins, G.S., Daubar, I., Dehant, V., Drilleau, M., Fillingim, M., Folkner, W., Garcia, R.F., Garvin, J., Grant, J., Grott, M., Grygorczuk, J., Hudson, T., Irving, J.C. E., Kargl, G., Kawamura, T., Kedar, S., King, S., Knapmeyer-Endrun, B., Knapmeyer, M., Lemmon, M., Lorenz, R., Maki, J.N., Margerin, L., McLennan, S.M., Michaut, C., Mimoun, D., Mittelholz, A., Mocquet, A., Morgan, P., Mueller, N.T., Murdoch, N., Nagihara, S., Newman, C., Nimmo, F., Panning, M., Pike, W.T., Plesa, A.-C., Rodriguez, S., Rodriguez-Manfredi, J.A., Russell, C.T., Schmerr, N., Siegler, M., Stanley, S., Stutzmann, E., Teanby, N., Tromp, J., van Driel, M., Warner, N., Weber, R., Wieczorek, M., 2020. Initial results from the InSight mission on Mars. Nat. Geosci. 13, 183–189. https://doi.org/10.1038/s41561-020-0544-y.

Banfield, D., Spiga, A., Newman, C., Forget, F., Lemmon, M., Lorenz, R., Murdoch, N., Viudez-Moreiras, D., Pla-Garcia, J., Garcia, R.F., Lognonné, P., Karatekin, Ö., Perrin, C., Martire, L., Teanby, N., Hove, B.V., Maki, J.N., Kenda, B., Mueller, N.T., Rodriguez, S., Kawamura, T., McClean, J.B., Stott, A.E., Charalambous, C., Millour, E., Johnson, C.L., Mittelholz, A., Määttänen, A., Lewis, S.R., Clinton, J., Stähler, S.C., Ceylan, S., Giardini, D., Warren, T., Pike, W.T., Daubar, I., Golombek, M., Rolland, L., Widmer-Schnidrig, R., Mimoun, D., Beucler, É., Jacob, A., Lucas, A., Baker, M., Ansan, V., Hurst, K., Mora-Sotomayor, L., Navarro, S., Torres, J., Lepinette, A., Molina, A., Marin-Jimenez, M., Gomez-Elvira, J., Peinado, V., Rodriguez-Manfredi, J.-A., Carcich, B.T., Sackett, S., Russell, C.T., Spohn, T., Smrekar, S.E., Banerdt, W.B., 2020. The atmosphere of Mars as observed by InSight. Nat. Geosci. 13, 190–198. https://doi.org/10.1038/s41561-020-0534-0.

Bechtel, B., Wiesner, S., Zakšek, K., 2014. Estimation of dense time series of urban air temperatures from multitemporal geostationary satellite data. IEEE J. Sel. Top. Appl. Earth Obs. Rem. Sens. 7, 4129–4137. https://doi.org/10.1109/JSTARS.2014.2322449.

Bechtel, B., Zakšek, K., Oßenbrügge, J., Kaveckis, G., Böhner, J., 2017. Towards a satellite based monitoring of urban air temperatures. Sustain. Cities Soc. 34, 22–31. https://doi.org/10.1016/j.scs.2017.05.018.

Christensen, P.R., Jakosky, B.M., Kieffer, H.H., Malin, M.C., McSween Jr., H.Y., Nealson, K., Mehall, G.L., Silverman, S.H., Ferry, S., Caplinger, M., Ravine, M., 2004. The thermal emission imaging System (THEMIS) for the mars 2001 Odyssey mission. Space Sci. Rev. 110, 85–130. https://doi.org/10.1023/B:SPAC.0000021008.16305.94.

Davy, R., Davis, J.A., Taylor, P.A., Lange, C.F., Weng, W., Whiteway, J., Gunnlaugson, H. P., 2010. Initial analysis of air temperature and related data from the Phoenix MET station and their use in estimating turbulent heat fluxes. J. Geophys. Res.: Planets 115, E00–E13. https://doi.org/10.1029/2009JE003444.

Duan, S.-B., Li, Z.-L., Tang, B.-H., Wu, H., Tang, R., Bi, Y., Zhou, G., 2014. Estimation of diurnal cycle of land surface temperature at high temporal and spatial resolution from clear-sky MODIS data. Remote Sens. 6, 3247–3262. https://doi.org/10.3390/rs6043247.

Duan, S.-B., Li, Z.-L., Wang, N., Wu, H., Tang, B.-H., 2012. Evaluation of six land-surface diurnal temperature cycle models using clear-sky in situ and satellite data. Rem. Sens. Environ. 124, 15–25. https://doi.org/10.1016/j.rse.2012.04.016.

Farley, K.A., Williford, K.H., Stack, K.M., Bhartia, R., Chen, A., de la Torre, M., Hand, K., Goreva, Y., Herd, C.D.K., Hueso, R., Liu, Y., Maki, J.N., Martinez, G., Moeller, R.C., Nelessen, A., Newman, C.E., Nunes, D., Ponce, A., Spanovich, N., Willis, P.A., Beegle, L.W., Bell, J.F., Brown, A.J., Hamran, S.-E., Hurowitz, J.A., Maurice, S., Paige, D.A., Rodriguez-Manfredi, J.A., Schulte, M., Wiens, R.C., 2020. Mars 2020 mission overview. Space Sci. Rev. 216, 142. https://doi.org/10.1007/s11214-020-00762-y.

Giuranna, M., Wolkenberg, P., Grassi, D., Aronica, A., Aoki, S., Scaccabarozzi, D., Saggin, B., Formisano, V., 2021. The current weather and climate of mars: 12 years of atmospheric monitoring by the planetary fourier spectrometer on mars express. Icarus 353, 113406. https://doi.org/10.1016/j.icarus.2019.113406.

Gómez-Elvira, J., Armiens, C., Carrasco, I., Genzer, M., Gómez, F., Haberle, R., Hamilton, V.E., Harri, A.-M., Kahanpää, H., Kemppinen, O., Lepinette, A., Martín Soler, J., Martín-Torres, J., Martínez-Frías, J., Mischna, M., Mora, L., Navarro, S., Newman, C., de Pablo, M.A., Peinado, V., Polkko, J., Rafkin, S.C.R., Ramos, M., Rennó, N.O., Richardson, M., Rodríguez-Manfredi, J.A., Romeral Planelló, J.J., Sebastián, E., de la Torre Juárez, M., Torres, J., Urquí, R., Vasavada, A.R., Verdasca, J., Zorzano, M.-P., 2014. Curiosity's rover environmental monitoring station: overview of the first 100 sols. J. Geophys. Res.: Planets 119, 1680–1688. https://doi.org/10.1002/2013JE004576.

Gómez-Elvira, J., Armiens, C., Castañer, L., Domínguez, M., Genzer, M., Gómez, F., Haberle, R., Harri, A.-M., Jiménez, V., Kahanpää, H., Kowalski, L., Lepinette, A., Martín, J., Martínez-Frías, J., McEwan, I., Mora, L., Moreno, J., Navarro, S., de Pablo, M.A., Peinado, V., Peña, A., Polkko, J., Ramos, M., Renno, N.O., Ricart, J., Richardson, M., Rodríguez-Manfredi, J., Romeral, J., Sebastián, E., Serrano, J., de la Torre Juárez, M., Torres, J., Torrero, F., Urquí, R., Vázquez, L., Velasco, T., Verdasca, J., Zorzano, M.-P., Martín-Torres, J., 2012. REMS: the environmental sensor suite for the mars science laboratory rover. Space Sci. Rev. 170, 583–640. https://doi.org/10.1007/s11214-012-9921-1.

Göttsche, F.-M., Olesen, F.-S., 2009. Modelling the effect of optical thickness on diurnal cycles of land surface temperature. Rem. Sens. Environ. 113, 2306–2316. https://doi.org/10.1016/j.rse.2009.06.006.

Göttsche, F.-M., Olesen, F.S., 2001. Modelling of diurnal cycles of brightness temperature extracted from METEOSAT data. Rem. Sens. Environ. 76, 337–348. https://doi.org/10.1016/S0034-4257(00)00214-5.

Grima, C., Kofman, W., Mouginot, J., Phillips, R.J., Hérique, A., Biccari, D., Seu, R., Cutigni, M., 2009. North polar deposits of Mars: extreme purity of the water ice. Geophys. Res. Lett. 36. https://doi.org/10.1029/2008GL036326.

Helbert, J., Arnold, G., Benkhoff, J., Hirsch, H., Maturilli, A., Formisano, V., Giuranna, M., 2006. Comparison of surface temperatures measured by the planetary fourier spectrometer (PFS) on mars express with predictions from the Berlin mars near surface thermal model (BMST) for the BEAGLE 2 landing site in isidis Planitia. Adv. Space Res. 38, 709–712. https://doi.org/10.1016/j.asr.2005.05.007.

Hess, S.L., Henry, R.M., Kuettner, J., Leovy, C.B., Ryan, J.A., 1972. Meteorology experiments: the viking mars lander. Icarus 16, 196–204. https://doi.org/10.1016/0019-1035(72)90146-7.

Hess, S.L., Henry, R.M., Leovy, C.B., Ryan, J.A., Tillman, J.E., 1977. Meteorological results from the surface of mars: viking 1 and 2. J. Geophys. Res. 82, 4559–4574. https://doi.org/10.1029/JS082i028p04559.

Holmes, T.R.H., Crow, W.T., Hain, C., Anderson, M.C., Kustas, W.P., 2015. Diurnal temperature cycle as observed by thermal infrared and microwave radiometers. Rem. Sens. Environ. 158, 110–125. https://doi.org/10.1016/j.rse.2014.10.031.

Hong, F., Zhan, W., Göttsche, F.-M., Liu, Z., Dong, P., Fu, H., Huang, F., Zhang, X., 2022. A global dataset of spatiotemporally seamless daily mean land surface temperatures: generation, validation, and analysis. Earth Syst. Sci. Data 14, 3091–3113. https://doi.org/10.5194/essd-14-3091-2022.

Hong, F., Zhan, W., Göttsche, F.-M., Liu, Z., Zhou, J., Huang, F., Lai, J., Li, M., 2018. Comprehensive assessment of four-parameter diurnal land surface temperature cycle models under clear-sky. ISPRS J. Photogrammetry Remote Sens. 142, 190–204. https://doi.org/10.1016/j.isprsjprs.2018.06.008.

Huang, F., Zhan, W., Duan, S.-B., Ju, W., Quan, J., 2014. A generic framework for modeling diurnal land surface temperatures with remotely sensed thermal observations under clear sky. Rem. Sens. Environ. 150, 140–151. https://doi.org/10.1016/j.rse.2014.04.022.

Inamdar, A.K., French, A., Hook, S., Vaughan, G., Luckett, W., 2008. Land surface temperature retrieval at high spatial and temporal resolutions over the southwestern United States. J. Geophys. Res. Atmos. 113. https://doi.org/10.1029/2007JD009048.

Iqbal, M., 1983. An Introduction to Solar Radiation.

Jin, S., Zhang, T., 2014. Automatic detection of impact craters on Mars using a modified adaboosting method. Planet. Space Sci. 99, 112–117. https://doi.org/10.1016/j.pss.2014.04.021.

Kavulich, M.J., Szunyogh, I., Gyarmati, G., Wilson, R.J., 2013. Local dynamics of baroclinic waves in the martian atmosphere. J. Atmos. Sci. 70, 3415–3447. https://doi.org/10.1175/JAS-D-12-0262.1.

Kleinböhl, A., Schofield, J.T., Kass, D.M., Abdou, W.A., Backus, C.R., Sen, B., Shirley, J. H., Lawson, W.G., Richardson, M.I., Taylor, F.W., Teanby, N.A., McCleese, D.J.,

2009. Mars Climate Sounder limb profile retrieval of atmospheric temperature, pressure, and dust and water ice opacity. J. Geophys. Res.: Planets 114. https://doi.org/10.1029/2009JE003358.
Lemmon, M., 2023. Mars Science Laboratory aerosol optical depths. https://doi.org/10.17632/tbh3pg39xc.2.
Li, X., Yao, W., Wang, H., 2023. Martian subsurface water ice prediction at the Tianwen-1 mission landing site. Icarus 389, 115268. https://doi.org/10.1016/j.icarus.2022.115268.
Li, Y., Liu, J., Jin, S., 2021. Horizontal internal gravity waves in the mars upper atmosphere from MAVEN ACC and NGIMS measurements. J. Geophys. Res.: Space Phys. 126, e2020JA028378. https://doi.org/10.1029/2020JA028378.
Martínez, G.M., Newman, C.N., De Vicente-Retortillo, A., Fischer, E., Renno, N.O., Richardson, M.I., Fairén, A.G., Genzer, M., Guzewich, S.D., Haberle, R.M., Harri, A.-M., Kemppinen, O., Lemmon, M.T., Smith, M.D., de la Torre-Juárez, M., Vasavada, A. R., 2017. The modern near-surface martian climate: a review of in-situ meteorological data from viking to curiosity. Space Sci. Rev. 212, 295–338. https://doi.org/10.1007/s11214-017-0360-x.
Martínez, G.M., Rennó, N., Fischer, E., Borlina, C.S., Hallet, B., de la Torre Juárez, M., Vasavada, A.R., Ramos, M., Hamilton, V., Gomez-Elvira, J., Haberle, R.M., 2014. Surface energy budget and thermal inertia at Gale Crater: calculations from ground-based measurements. J. Geophys. Res.: Planets 119, 1822–1838. https://doi.org/10.1002/2014JE004618.
Martínez, G.M., Vicente-Retortillo, A., Vasavada, A.R., Newman, C.E., Fischer, E., Rennó, N.O., Savijärvi, H., de la Torre, M., Ordóñez-Etxeberria, I., Lemmon, M.T., Guzewich, S.D., McConnochie, T.H., Sebastián, E., Hueso, R., Sánchez-Lavega, A., 2021. The surface energy budget at Gale Crater during the first 2500 sols of the mars science laboratory mission. JGR Planets 126. https://doi.org/10.1029/2020JE006804.
McCleese, D.J., Schofield, J.T., Taylor, F.W., Calcutt, S.B., Foote, M.C., Kass, D.M., Leovy, C.B., Paige, D.A., Read, P.L., Zurek, R.W., 2007. Mars Climate Sounder: an investigation of thermal and water vapor structure, dust and condensate distributions in the atmosphere, and energy balance of the polar regions. J. Geophys. Res.: Planets 112. https://doi.org/10.1029/2006JE002790.
Mellon, M.T., Sizemore, H.G., Heldmann, J.L., McKay, C.P., Stoker, C.R., 2024. The habitability conditions of possible Mars landing sites for life exploration. Icarus 408, 115836. https://doi.org/10.1016/j.icarus.2023.115836.
Michalski, J.R., Onstott, T.C., Mojzsis, S.J., Mustard, J., Chan, Q.H.S., Niles, P.B., Johnson, S.S., 2018. The Martian subsurface as a potential window into the origin of life. Nat. Geosci. 11, 21–26. https://doi.org/10.1038/s41561-017-0015-2.
Moore, H.J., Hutton, R.E., Clow, G.D., Spitzer, C.R., 1987. Physical properties of the surface materials at the Viking landing sites on Mars. Professional Paper. https://doi.org/10.3133/pp1389.
Moore, H.J., Hutton, R.E., Scott, R.F., Spitzer, C.R., Shorthill, R.W., 1977. Surface materials of the Viking landing sites. J. Geophys. Res. 82, 4497–4523. https://doi.org/10.1029/JS082i028p04497.
Mueller, N., Piqueux, S., Lemmon, M., Maki, J., Lorenz, R.D., Grott, M., Spohn, T., Smrekar, S.E., Knollenberg, J., Hudson, T.L., Krause, C., Millour, E., Forget, F., Golombek, M., Hagermann, A., Attree, N., Siegler, M., Banerdt, W.B., 2021. Near surface properties of martian regolith derived from InSight HP3-RAD temperature observations during phobos transits. Geophys. Res. Lett. 48, e2021GL093542. https://doi.org/10.1029/2021GL093542.
Munguira, A., Hueso, R., Sánchez-Lavega, A., de la Torre-Juarez, M., Martínez, G.M., Newman, C.E., Sebastian, E., Lepinette, A., Vicente-Retortillo, A., Chide, B., Lemmon, M.T., Bertrand, T., Lorenz, R.D., Banfield, D., Gómez-Elvira, J., Martín-Soler, J., Navarro, S., Pla-García, J., Rodríguez-Manfredi, J.A., Romeral, J., Smith, M. D., Torres, J., 2023. Near surface atmospheric temperatures at Jezero from mars 2020 MEDA measurements. J. Geophys. Res.: Planets 128, e2022JE007559. https://doi.org/10.1029/2022JE007559.
Piqueux, S., Edwards, C.S., Christensen, P.R., 2008. Distribution of the ices exposed near the south pole of Mars using Thermal Emission Imaging System (THEMIS) temperature measurements. J. Geophys. Res.: Planets 113. https://doi.org/10.1029/2007JE003055.
Piqueux, S., Kass, D.M., Kleinböhl, A., Slipski, M., Hayne, P.O., McCleese, D.J., Schofield, J.T., Heavens, N., 2023. Mars thermal inertia and surface temperatures by the Mars Climate Sounder. Icarus, 115851. https://doi.org/10.1016/j.icarus.2023.115851.
Piqueux, S., Müller, N., Grott, M., Siegler, M., Millour, E., Forget, F., Lemmon, M., Golombek, M., Williams, N., Grant, J., Warner, N., Ansan, V., Daubar, I., Knollenberg, J., Maki, J., Spiga, A., Banfield, D., Spohn, T., Smrekar, S., Banerdt, B., 2021. Soil thermophysical properties near the InSight lander derived from 50 sols of radiometer measurements. J. Geophys. Res.: Planets 126, e2021JE006859. https://doi.org/10.1029/2021JE006859.
Rodriguez-Manfredi, J.A., de la Torre Juarez, M., Sanchez-Lavega, A., Hueso, R., Martinez, G., Lemmon, M.T., Newman, C.E., Munguira, A., Hieta, M., Tamppari, L. K., Polkko, J., Toledo, D., Sebastian, E., Smith, M.D., Jaakonaho, I., Genzer, M., De Vicente-Retortillo, A., Viudez-Moreiras, D., Ramos, M., Saiz-Lopez, A., Lepinette, A., Wolff, M., Sullivan, R.J., Gomez-Elvira, J., Apestigue, V., Conrad, P.G., Del Rio-Gaztelurrutia, T., Murdoch, N., Arruego, I., Banfield, D., Boland, J., Brown, A.J., Ceballos, J., Dominguez-Pumar, M., Espejo, S., Fairén, A.G., Ferrandiz, R., Fischer, E., Garcia-Villadangos, M., Gimenez, S., Gomez-Gomez, F., Guzewich, S.D., Harri, A.-M., Jimenez, J.J., Jimenez, V., Makinen, T., Marin, M., Martin, C., Martin-Soler, J., Molina, A., Mora-Sotomayor, L., Navarro, S., Peinado, V., Perez-Grande, I., Pla-Garcia, J., Postigo, M., Prieto-Ballesteros, O., Rafkin, S.C.R., Richardson, M.I., Romeral, J., Romero, C., Savijärvi, H., Schofield, J.T., Torres, J., Urqui, R., Zurita, S., 2023. The diverse meteorology of Jezero crater over the first 250 sols of Perseverance on Mars. Nat. Geosci. 16, 19–28. https://doi.org/10.1038/s41561-022-01084-0.
Rodriguez-Manfredi, J.A., De La Torre Juárez, M., Alonso, A., Apéstigue, V., Arruego, I., Atienza, T., Banfield, D., Boland, J., Carrera, M.A., Castañer, L., Ceballos, J., Chen-Chen, H., Cobos, A., Conrad, P.G., Cordoba, E., Del Río-Gaztelurrutia, T., De Vicente-Retortillo, A., Domínguez-Pumar, M., Espejo, S., Fairen, A.G., Fernández-Palma, A., Ferrándiz, R., Ferri, F., Fischer, E., García-Manchado, A., García-Villadangos, M., Genzer, M., Giménez, S., Gómez-Elvira, J., Gómez, F., Guzewich, S.D., Harri, A.-M., Hernández, C.D., Hieta, M., Hueso, R., Jaakonaho, I., Jiménez, J.J., Jiménez, V., Larman, A., Leiter, R., Lepinette, A., Lemmon, M.T., López, G., Madsen, S.N., Mäkinen, T., Marín, M., Martín-Soler, J., Martínez, G., Molina, A., Mora-Sotomayor, L., Moreno-Álvarez, J.F., Navarro, S., Newman, C.E., Ortega, C., Parrondo, M.C., Peinado, V., Peña, A., Pérez-Grande, I., Pérez-Hoyos, S., Pla-García, J., Polkko, J., Postigo, M., Prieto-Ballesteros, O., Rafkin, S.C.R., Ramos, M., Richardson, M.I., Romeral, J., Romero, C., Runyon, K.D., Saiz-Lopez, A., Sánchez-Lavega, A., Sard, I., Schofield, J.T., Sebastian, E., Smith, M.D., Sullivan, R.J., Tamppari, L.K., Thompson, A.D., Toledo, D., Torrero, F., Torres, J., Urquí, R., Velasco, T., Viúdez-Moreiras, D., Zurita, S., The MEDA team, 2021. The mars environmental dynamics analyzer, MEDA. A suite of environmental sensors for the mars 2020 mission. Space Sci. Rev. 217, 48. https://doi.org/10.1007/s11214-021-00816-9.
Savijärvi, H.I., Martinez, G.M., Vicente-Retortillo, A., Harri, A.-M., 2022. Surface energy budget at Curiosity through observations and column modeling. Icarus 376, 114900. https://doi.org/10.1016/j.icarus.2022.114900.
Schädlich, S., Göttsche, F.M., Olesen, F.-S., 2001. Influence of land surface parameters and atmosphere on METEOSAT brightness temperatures and generation of land surface temperature maps by temporally and spatially interpolating atmospheric correction. Rem. Sens. Environ. 75, 39–46. https://doi.org/10.1016/S0034-4257(00)00154-1.
Schofield, J.T., Barnes, J.R., Crisp, D., Haberle, R.M., Larsen, S., Magalhães, J.A., Murphy, J.R., Seiff, A., Wilson, G., 1997. The mars pathfinder atmospheric structure investigation/meteorology (ASI/MET) experiment. Science 278, 1752–1758. https://doi.org/10.1126/science.278.5344.1752.
Sebastián, E., Martínez, G., Ramos, M., Pérez-Grande, I., Sobrado, J., Rodríguez Manfredi, J.A., 2021. Thermal calibration of the MEDA-TIRS radiometer onboard NASA's Perseverance rover. Acta Astronaut. 182, 144–159. https://doi.org/10.1016/j.actaastro.2021.02.006.
Shirley, J.H., McConnochie, T.H., Kass, D.M., Kleinböhl, A., Schofield, J.T., Heavens, N. G., McCleese, D.J., Benson, J., Hinson, D.P., Bandfield, J.L., 2015. Temperatures and aerosol opacities of the Mars atmosphere at aphelion: validation and inter-comparison of limb sounding profiles from MRO/MCS and MGS/TES. Icarus 251, 26–49. https://doi.org/10.1016/j.icarus.2014.05.011.
Smith, M.D., 2019a. THEMIS observations of the 2018 mars global dust storm. J. Geophys. Res.: Planets 124, 2929–2944. https://doi.org/10.1029/2019JE006107.
Smith, M.D., 2019b. Local time variation of water ice clouds on Mars as observed by THEMIS. Icarus 333, 273–282. https://doi.org/10.1016/j.icarus.2019.06.009.
Smith, M.D., 2008. Spacecraft observations of the martian atmosphere. Annu. Rev. Earth Planet Sci. 36, 191–219. https://doi.org/10.1146/annurev.earth.36.031207.124334.
Smith, M.D., 2004. Interannual variability in TES atmospheric observations of Mars during 1999–2003. Icarus 167, 148–165. https://doi.org/10.1016/j.icarus.2003.09.010.
Smith, M.D., Bandfield, J.L., Christensen, P.R., Richardson, M.I., 2003. Thermal Emission Imaging System (THEMIS) infrared observations of atmospheric dust and water ice cloud optical depth. J. Geophys. Res.: Planets 108. https://doi.org/10.1029/2003JE002115.
Smith, M.D., Bougher, S.W., Encrenaz, T., Forget, F., Kleinböhl, A., 2017. Thermal structure and composition. In: Haberle, R.M., Clancy, R.T., Forget, F., Smith, M.D., Zurek, R.W. (Eds.), The Atmosphere and Climate of Mars. Cambridge University Press, pp. 42–75. https://doi.org/10.1017/9781139060172.004.
Smith, M.D., Martínez, G.M., Sebastián, E., Lemmon, M.T., Wolff, M.J., Apéstigue, V., Arruego, I., Toledo, D., Viúdez-Moreiras, D., Rodriguez-Manfredi, J.A., Juarez, M. de la T., 2023. Diurnal and seasonal variations of aerosol optical depth observed by MEDA/TIRS at Jezero crater, mars. J. Geophys. Res.: Planets 128, e2022JE007560. https://doi.org/10.1029/2022JE007560.
Soffen, G.A., 1977. The viking project. J. Geophys. Res. 82, 3959–3970. https://doi.org/10.1029/JS082i028p03959.
Soffen, G.A., 1976. Scientific results of the viking missions. Science 194, 1274–1276. https://doi.org/10.1126/science.194.4271.1274.
Soffen, G.A., Snyder, C.W., 1976. The first viking mission to mars. Science 193, 759–766. https://doi.org/10.1126/science.193.4255.759.
Spohn, T., Grott, M., Smrekar, S.E., Knollenberg, J., Hudson, T.L., Krause, C., Müller, N., Jänchen, J., Börner, A., Wippermann, T., Krömer, O., Lichtenheldt, R., Wisniewski, L., Grygorczuk, J., Fittock, M., Rheershemius, S., Spröwitz, T., Kopp, E., Walter, I., Plesa, A.C., Breuer, D., Morgan, P., Banerdt, W.B., 2018. The heat flow and physical properties package (HP3) for the InSight mission. Space Sci. Rev. 214, 96. https://doi.org/10.1007/s11214-018-0531-4.
Stcherbinine, A., Edwards, C.S., Smith, M.D., Wolff, M.J., Haberle, C., Al Tunaiji, E., Smith, N.M., Saboi, K., Anwar, S., Lange, L., Christensen, P.R., 2023. Diurnal and seasonal mapping of martian ices with EMIRS. Geophys. Res. Lett. 50, e2023GL103629. https://doi.org/10.1029/2023GL103629.
Sutton, J.L., Leovy, C.B., Tillman, J.E., 1978. Diurnal variations of the martian surface layer meteorological parameters during the first 45 sols at two viking lander sites. J. Atmos. Sci. 35, 2346–2355. https://doi.org/10.1175/1520-0469(1978)035<2346:DVOTMS>2.0.CO;2.

Temel, O., Senel, C.B., Spiga, A., Murdoch, N., Banfield, D., Karatekin, O., 2022. Spectral analysis of the martian atmospheric turbulence: InSight observations. Geophys. Res. Lett. 49, e2022GL099388. https://doi.org/10.1029/2022GL099388.

Tillman, J.E., 1989. Viking lander MET bundle. https://doi.org/10.17189/1518948.

Van den Bergh, F., Van Wyk, M.A., Van Wyk, B.J., 2006. Comparison of data-driven and model-driven approaches to brightness temperature diurnal cycle interpolation. Presented at the 17th Annual Symposium of the Pattern Recognition Association of South Africa, Parys, South Africa.

Vasavada, A.R., 2022. Mission overview and scientific contributions from the mars science laboratory curiosity rover after eight years of surface operations. Space Sci. Rev. 218, 14. https://doi.org/10.1007/s11214-022-00882-7.

Vasavada, A.R., Piqueux, S., Lewis, K.W., Lemmon, M.T., Smith, M.D., 2017. Thermophysical properties along *Curiosity*'s traverse in Gale crater, Mars, derived from the REMS ground temperature sensor. Icarus 284, 372–386. https://doi.org/10.1016/j.icarus.2016.11.035.

Vollmer, M., Gedzelman, S.D., 2006. Colours of the Sun and Moon: the role of the optical air mass. Eur. J. Phys. 27, 299. https://doi.org/10.1088/0143-0807/27/2/013.

Wilson, R.J., Smith, M.D., 2006. The effects of atmospheric dust on the seasonal variation of Martian surface temperature. Presented at the the Second International Workshop on the Mars Atmosphere: Modelling and Observations. Granada, Spain.

Wolfe, C.A., Edwards, C.S., Smith, M.D., Christensen, P.R., 2023. Constraining changes in surface dust thickness on mars using diurnal surface temperature observations from EMIRS. J. Geophys. Res.: Planets 128, e2023JE007794. https://doi.org/10.1029/2023JE007794.

Wolkenberg, P., Smith, M.D., Formisano, V., Sindoni, G., 2011. Comparison of PFS and TES observations of temperature and water vapor in the martian atmosphere. Icarus 215, 628–638. https://doi.org/10.1016/j.icarus.2011.07.032.

Xiao, J., Chow, K.-C., Chan, K., 2019. Dynamical processes of dust lifting in the northern mid-latitude region of Mars during the dust storm season. Icarus 317, 94–103. https://doi.org/10.1016/j.icarus.2018.07.020.

Zhan, W., Zhou, J., Ju, W., Li, M., Sandholt, I., Voogt, J., Yu, C., 2014. Remotely sensed soil temperatures beneath snow-free skin-surface using thermal observations from tandem polar-orbiting satellites: an analytical three-time-scale model. Rem. Sens. Environ. 143, 1–14. https://doi.org/10.1016/j.rse.2013.12.004.

Zurek, R.W., Smrekar, S.E., 2007. An overview of the Mars Reconnaissance Orbiter (MRO) science mission. J. Geophys. Res. 112, E05S01. https://doi.org/10.1029/2006JE002701.